Measurement of the transverse spin correlations in the decay $Z^0 \to \tau^+\tau^-$ [1]

Federico Sánchez Nieto
Universitat Autònoma de Barcelona
Institut de Física d'Altes Energies
Edifici Cn
E-08193 Bellaterra (Barcelona) Spain

3-December-1996

[1] Ph Dissertation

A mis padres.
A mis hermanos.
A Patricia.

Acknowledgements

I would like to thank Enrique Fernández first, who gave me the opportunity to work in the IFAE and join the ALEPH collaboration. The offer to join the IFAE group came just at the time when the τCF project in Sevilla was cancelled, and gave me the possibility to continue working in the High Energy Physics field when the rest of the options were almost discarded. I would like to thank him for the confidence he deposited on me when he offered me the possibility of working in the maintenance and upgrade of the BCAL detector. I also appreciate the effort he did to help me in this analysis; he has many important responsibilities but he always managed to find the time to listen to me.

I cannot express all my gratitude to Mokhtar Chmeissani. He found a disorganized and shy graduated student and made a physicist from him. He has taught me everything I know about hardware. He showed me how to be careful and secure with my work, how to take responsibilities and how to work with other people. He has supported me in all my initiatives, he has listened to me in all the bad moments of doing a thesis. More than my "boss" in the BCAL project, he has been my teacher, my friend, my supervisor and my supporter. He tried always to protect me and to give me all the credit for work we did together.

I should not forget about the people who helped me at the beginning in Sevilla, Enrique González and Isabel Gallardo. They gave me the possibility of working in particle physics in the University of Sevilla were there was not any group investigating in this field. For almost a year, Enrique González was flying from Madrid to Sevilla to follow our work. I appreciate very much his patience and dedication. I would like to mention the other students in the τCF at Sevilla, Juan Ramón, Ricardo, Ramón and Jose Ignacio. I will always remember the good and bad moments we spent together in this long room in ABENGOA.

Special acknowledgement goes to Anna Pascual, Cristobal Padilla and Frederic Teubert who were always ready to listen to this "depressive" andalusian guy. I will acknowledge specially Cristobal, we conspired together for almost three years in the IFAE corridors, we shared the idea that anything can be improved.

I would like to thank all the people who have worked in the IFAE during the last 3 years. I cannot mention all of them, but I can say I learnt something from everyone, the engineers, the students, and the seniors working on any project at the IFAE. I would like to make a special mention to Mateo Cavalli-Sforza, he listened to me many times regardless of the fact that we were not working together, I really

appreciate all his advise although I should confess I didn't always follow them. I want to thanks the hospitality of all the catalans at CERN, Ramón Miquel, Lluisa Mir, Pere Mató. They made the stays at CERN much more comfortable. I have bothered them many times with my problems in the analysis or with the BCAL software.

I also have the pleasure to acknowledge Lluis Garrido, my office-mate. He has listened many times about this "aplanarities" business patiently, and helped me in many of the breaking points you find in an analysis.

I want to thanks the unconditional support and friendship I received from Juanjo Goméz-Cadenas. He is one the best "motards" and friends I knew and I learnt thousand of things about physics from him and he has helped me with his enthusiasm many times.

During my work in BCAL I have been working closely with the ALEPH ONLINE group who were always kind in answering my questions and discussing with me about all the aspects related to the DAQ. I want to mention all the people working in the BCAL^{++} project, Alison, Pilar, Gonzalo,... we shared the enthusiasm in doing and understanding a new detector. It has been a pleasure to work with all of them.

It is not possible to value the support of my family. They understood a long time ago that I like to do physics and they helped me in getting it. I know it has been hard for them to be separated one thousand kilometers, but they never complained. I am indebted to my parents, they showed me to be responsible and passionate in my work. I spent my life surrounded by books which gave me the "need" of knowledge. This "need" was kept and promoted by them. My sister Beatriz has been a model for a long time, she opened the physics line in my family that I followed. I missed my sister Maria these four years, and I am sure she did too. My brother Alejandro has helped me in the distance in many ways he doesn't know but I do appreciate.

I would like to mentioned one person that has entered in my life less than one year ago. Patricia has become in these few months the most passionate supporter I have. She has suffered my trips to Geneva and the weekends I spent far from her in the laboratory and, in spite of that, she has helped me to keep the enthusiasm in everything I do.

Abstract

The measurement of the density matrix transverse spin correlation terms in the decay $Z^0 \to \tau^+\tau^-$ performed by the ALEPH at LEP is presented. In addition to the longitudinal polarization of each τ lepton produced in $e^+e^- \to \tau^+\tau^-$ interactions, there are two independent spin-spin correlations associated with the transverse (within the production plane) and normal (to the production plane) polarization components. A measurement of the transverse-transverse, $A_{\rm TT}$, and transverse-normal, $A_{\rm TN}$, τ spin correlations in the decay $Z^0 \to \tau^+\tau^-$ is presented based on the aplanarity angle of the decay products of both taus. Based on 80 pb^{-1} of data collected by ALEPH in 1992, 1993 and 1994 on the peak of the Z resonance, the results are $A_{\rm TT} = 1.06 \pm 0.13(stat) \pm 0.05(syst)$, and $A_{\rm TN} = 0.08 \pm 0.13(stat) \pm 0.04(syst)$. These values are in agreement with the Standard Model predictions, $A_{\rm TT} = 0.989$ and $A_{\rm TN} = 0$.

Resumen

La primera medida de la correlación entre las componentes transversas de los espines de los leptones τ en la desintegración $Z^0 \to \tau\tau$ se ha realizado usando el detector ALEPH de LEP. Además de la polarizaci'on longitudinal del leptón τ en el proceso $e^+e^- \to \tau^-\tau^+$, ya medidas por los experimentos de LEP, existen dos correlaciones ente las componentes transversas (contenidas en el plano de producción del estado final) y normales (perpendiculares al plano de producción) de sus espines. Esta es la primera medida realizada de las correlaciones entre las componentes transversa-transversa, A_{TT}, y transversa-normal, A_{TN}. La medida se ha realizado utilizando las asimetrías en el ángulo aplanar entre los productos de desintegración de los dos leptones τ en base a una luminosidad total de 80 pb^{-1} recogida por el detector ALEPH de LEP entre los años 1992 a 1994 con una energía centro de masa igual a la masa del bosón Z^0. Los resultados obtenidos son: $A_{\rm TT} = 1.06 \pm 0.13(stat) \pm 0.05(syst)$, and $A_{\rm TN} = 0.08 \pm 0.13(stat) \pm 0.04(syst)$. Ambos valores están en buen acuerdo con las predicciones de la teoría Modelo Standar, $A_{\rm TT} = 0.989$ y $A_{\rm TN} = 0$.

Contents

List of Figures

List of Tables

Chapter 1

Introduction

The longitudinal polarization of the taus produced in the reaction $e^+e^- \to \tau^+\tau^-$ at the Z^0 resonance has been widely studied in all the LEP experiments [1, 2, 3, 4]. As a result, the $Z{-}e$ and $Z{-}\tau$ couplings have been precisely measured. The measurements provide a stringent test of the electroweak Standard Model. In the context of this theory, they give a value of the weak mixing parameter, $\sin^2_{\rm eff}\,\theta_{\rm W}$.

In addition to the longitudinal spin polarization and correlation of the τ leptons, there are two independent spin-spin correlations associated with the transverse (within the production plane) and normal (to the production plane) polarization components. These correlations are predicted by the Standard Model. The feasibility of extracting these transverse spin correlations from the $\tau^+\tau^-$ production cross section at LEP has been shown [5]. The first evidence of a correlation different from zero has been obtained by the DELPHI collaboration [6].

The presence of transverse spin correlations is a consequence of the conservation of the angular momentum but their value depend on the coupling constants and may even be zero, through cancellations, for certain theoretical models. For example, a maximal parity violation vertex, such us $\gamma^\mu(1-\gamma^5)$, produces null transverse-transverse spin correlations.

The expected precision [5] to measure basic parameters of the Standard Model, like the electroweak mixing angle, which can be obtained from the measurement of transverse spin-spin correlations will never be competitive with the values obtained from the longitudinal spin polarization. However, the latter depends on a symmet-

rical manner of v_τ and a_τ, the tau vector and axial vector neutral current couplings, respectively, while the transverse-transverse spin correlation, $A_{\rm TT}$, is proportional to $|a_\tau|^2 - |v_\tau|^2$. Therefore its value alone will indicate which of these two couplings is larger. In any case, it is desirable to carry out a most general test of the coupling structure of the theory. The transverse-normal spin correlation $A_{\rm TN}$ [7] is both a parity-odd and time-reversal-odd observable and is therefore zero in the Standard Model except for a very small contribution from the $\gamma - Z^0$ interference. In some extended models $A_{\rm TN}$ could get a contribution from CP-violating amplitudes. A value different from zero can be generated from imaginary parts in the electroweak couplings.

The outline of this thesis is as follows. Chapter 2 is devoted to describe the structure of Standard Model Theory, and to define the theoretical framework in which the measurement of the transverse spin correlations is done. The LEP accelerator and ALEPH detector in which the measurement is performed is described in Chapter 3. The Chapter 4 describes the criteria to select the events used to measure the transverse spin correlations. The method used to measure both transverse spin correlations and the results are described in Chapter 5. An overview of the systematic uncertainties are shown in Chapter 6. Finally, some Standard Model parameters are extracted in Chapter 7 from the measured transverse spin correlations.

Chapter 2

Theoretical Framework

2.1 The Standard Model

The Standard Model is a quantum field theory describing electroweak and strong interactions between particles.

The electroweak interaction is a local gauge theory first developed by Glashow, Weinberg and Salam. The electroweak interactions of quarks were introduced afterwards by Glashow, Iliopopulos and Maiani. This theory predicts the existence of neutral and charged currents mediated by the massive gauge bosons ($W^{\pm}, Z^0$).

The electromagnetic (mediated by photons) and the weak interactions (mediated by $W^{\pm}$) are unified in this theory requiring gauge invariance under the $SU(2)_Y \otimes U(1)_Y$ transformation group. A spontaneous symmetry breaking mechanism gives masses to the vector bosons without breaking the local gauge invariance. This mechanism predicts the existence of at least a new scalar particle, the Higgs, which has not yet been discovered.

The strong interaction (QCD) is a non-abelian gauge theory based in the colour group $SU(3)_C$. The eight gauge bosons (called gluons) obtained as a result of the local invariance are responsible for the strong interactions among quarks.

The standard Model contains the three following types of fields:

- Fermionic matter fields.
- Gauge fields,

- Higgs scalar fields.

The fermionic matter field is given by the leptons and quarks, which are organized in a 3-fold family structure:

$$\left[\begin{array}{cc}\nu_e & u\\ e^- & d\end{array}\right], \left[\begin{array}{cc}\nu_\mu & c\\ \mu^- & s\end{array}\right], \left[\begin{array}{cc}\nu_\tau & t\\ \tau^- & b\end{array}\right] \tag{2.1}$$

where (each quark appears in 3 different "colours")

$$\left[\begin{array}{cc}\nu_l & q_u\\ l^- & q_d\end{array}\right] \equiv \left(\begin{array}{c}\nu_l\\ l^-\end{array}\right)_L, \left(\begin{array}{c}q_u\\ q_d\end{array}\right)_L, \; l^-_R, \; (q_u)_R, \; (q_d)_R \tag{2.2}$$

plus the corresponding antiparticles, which are particles with the same masses but opposite quantum numbers.

The quantum numbers $\vec{T}$ and Y, the weak isospin and the weak hypercharge respectively, define the transformation properties of the fermions under the gauge group considered. The assignment of those quantum numbers are shown in Table 2.1.

The gauge fields are the mediators of the interactions between quarks and leptons. The weak interaction is mediated by the massive vector bosons $W^\pm$, Z^0. The electromagnetic interaction is mediated by one massless vector boson, the photon. The strong force is mediated by eight massless vector boson called gluon.

2.2 The Spontaneous symmetry breaking and the electroweak couplings

The interaction between the gauge bosons and the Higgs field generates the vector bosons masses. This matrix is not diagonal in $SU(2) \otimes U(1)$ generator fields (W^a_μ, B_μ):

$$\frac{1}{2}\left(\frac{g_2}{2}\nu\right)^2\left[(W^1)^2 + (W^2)^2)\right] + \frac{\nu^2}{4}(W^3_\mu, B_\mu)\left(\begin{array}{cc} g_2^2 & g_1 g_2\\ g_1 g_2 & g_1^2\end{array}\right)\left(\begin{array}{c} W^3_\mu\\ B_\mu\end{array}\right) \tag{2.3}$$

where g_2 and g_1 are respectively the $SU(2)$ and $U(1)$ coupling constants, and ν is the expected vacuum expectation value for the Higgs doublet.

Fermion	Y	T	T_3
$(\nu_l)_L$	-1/2	1/2	1/2
l_L	-1/2	1/2	-1/2
l_R	-1	0	0
$(u,c,t)_L$	1/6	1/2	1/2
$(d,s,b)_L$	1/6	1/2	-1/2
$(u,c,t)_R$	2/3	0	0
$(d,s,b)_R$	-1/3	0	0

Table 2.1: Isospin, T, and hypercharge, Y, for quarks and leptons.

The mass eigen-states for the gauge fields (W^a_μ, B_μ) are:

$$W^\pm_\mu = \frac{1}{\sqrt{2}}(W^1_\mu \pm W^2_\mu) \tag{2.4}$$

$$Z_\mu = \cos\theta_W W^3_\mu - \sin\theta_W B_\mu \tag{2.5}$$

$$A_\mu = \sin\theta_W W^3_\mu + \cos\theta_W B_\mu \tag{2.6}$$

where

$$M_W = \frac{1}{2} g_2 \nu \tag{2.7}$$

$$M_Z = \frac{1}{2}\sqrt{(g_2^2+g_1^2)}\nu \tag{2.8}$$

$$\cos\theta_W = \frac{M_W}{M_Z} = \frac{g_2}{\sqrt{(g_2^2+g_1^2)}} \tag{2.9}$$

$W_\mu^\pm$ and Z_μ are the fields associated with the gauge bosons $W^\pm$ and Z^0. The A_μ field is the photon field, which couples to the electron charge ($e = \sqrt{4\pi\alpha}$). The charge, e, can be defined as a function of the gauge coupling g_1 and g_2:

$$e = \frac{g_1 g_2}{\sqrt{(g_2^2+g_1^2)}} \tag{2.10}$$

$$g_2 = \frac{e}{\sin\theta_W}, \quad g_1 = \frac{e}{\cos\theta_W} \tag{2.11}$$

The axial vector and vector couplings can be written as a function of the parameters e, M_Z, M_W,

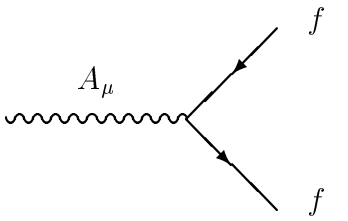

$ieQ_f\gamma_\mu$

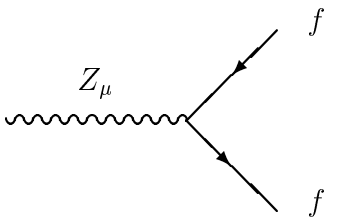

$i\ \frac{e}{2\cos\theta_W \sin\theta_W}\gamma_\mu(v_f - a_f\gamma_5)$

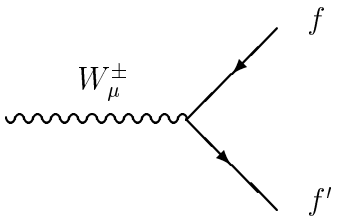

$i\ \frac{e}{\sqrt{2}\sin\theta_W}\gamma_\mu \mathrm{L}$

The coupling to the neutral currents are defined like follows:

$$\begin{aligned} \nu_f &= I_3^f - 2Q_f \sin^2\theta_W \\ a_f &= I_3^f \end{aligned} \tag{2.12}$$

where I_3^f is the isospin third component and Q_f is the fermion f charge.

2.3 $e^+e^- \to \tau^-\tau^+$ cross section

To the lowest order in perturbation theory, the Standard Model amplitude for the process,

$$e^+(k_1)e^-(k_2) \to \tau^-(p_1, s_1)\tau^+(p_2, s_2) \tag{2.13}$$

is the sum of the photon and Z^0 exchanges :

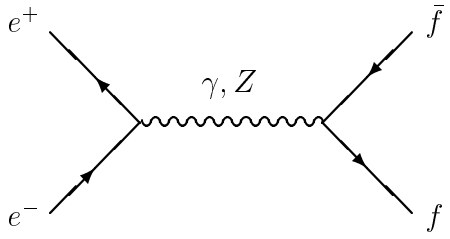

The amplitude for the process is:

$$M = M_\gamma + M_{Z^0} \tag{2.14}$$

$$M_\gamma = ie^2 \frac{Q_e Q_f}{s} \bar{\nu}(k_2)\gamma_\nu u(k_1)\bar{u}(p_1)\gamma^\nu \nu(p_2)$$

$$M_{Z^0} = \frac{i\ e^2}{4\sin^2\theta_W \cos^2\theta_W}\chi_0(s) \tag{2.15}$$

$$\bar{\nu}(k_2)\gamma_\nu(\nu_e - a_e\gamma_5)u(k_1)\bar{u}(p_1)(\nu_\tau - a_\tau\gamma_5)\gamma^\nu\nu(p_2) \tag{2.16}$$

The vector and axial vector coupling (a_τ, v_τ) are defined in equation 2.12. $\chi_0(s)$ is the Z^0 propagator,

$$\chi_0(s) = \frac{1}{s - M_Z^2 + iM_Z\Gamma_Z} \tag{2.17}$$

in the Breit Wigner approximation. The Z^0 width (Γ_Z) is defined as follows:

$$\Gamma_Z^0 = \sum_f N_C^f \frac{\alpha}{3} \frac{M_Z}{4 s_W^2 c_W^2} (v_f^2 + a_f^2) \tag{2.18}$$

where the colour factor (N_C^f) is 1 for leptons and 3 for quarks.

The initial $e^- e^+$ helicities are averaged in the supposition of unpolarized beams. The effect of the electron mass in the cross section is neglected, since the cross section will be computed around the Z^0 resonance ($\sqrt{s} = M_Z >> m_e$), but the final lepton masses are included in the cross section calculation to maintain the polarization effects.

To include the spin contribution explicitly, the cross-section for the reaction $e^+e^- \to \tau^+\tau^-$ will be computed for the spin directions, $\vec{s_1^*}$ and $\vec{s_2^*}$. $\vec{s_1^*}$ and $\vec{s_2^*}$ are unitary vectors in the τ^+ and τ^- rest frames, oriented in the direction of their momentum in the laboratory frame. In the lab frame, the z direction coincides with the τ^- momentum ($\vec{p}$), the y axis is defined by the vectorial product $\vec{p} \times \vec{k}$, where $\vec{k}$ is the direction of the beam electron. The reference frame is shown in Fig.2.1

The spin 4-vector of the final leptons are defined in this frame, as a function of the spin components in the τ rest frame :

$$\vec{s_1} = (\beta\gamma s_{1z}^*, s_{1x}^*, s_{1y}^*, \gamma s_{1z}^*) \tag{2.19}$$

$$\vec{s_2} = (-\beta\gamma s_{2z}^*, s_{2x}^*, s_{2y}^*, \gamma s_{2z}^*) \tag{2.20}$$

The projectors in the final lepton states with momentum p_i and spin in the $\vec{s_i^*}$ direction are,

$$\frac{1 + \gamma_5 \not{s}_1}{2} (\not{p}_1 + m), \quad \frac{1 + \gamma_5 \not{s}_2}{2} (-\not{p}_2 + m) \tag{2.21}$$

From the amplitudes (2.16) and the projectors (2.21), the differential cross-section for τ^-, τ^+ production with polarization vectors $\vec{s_1^*}$ and $\vec{s_2^*}$, may be written as,

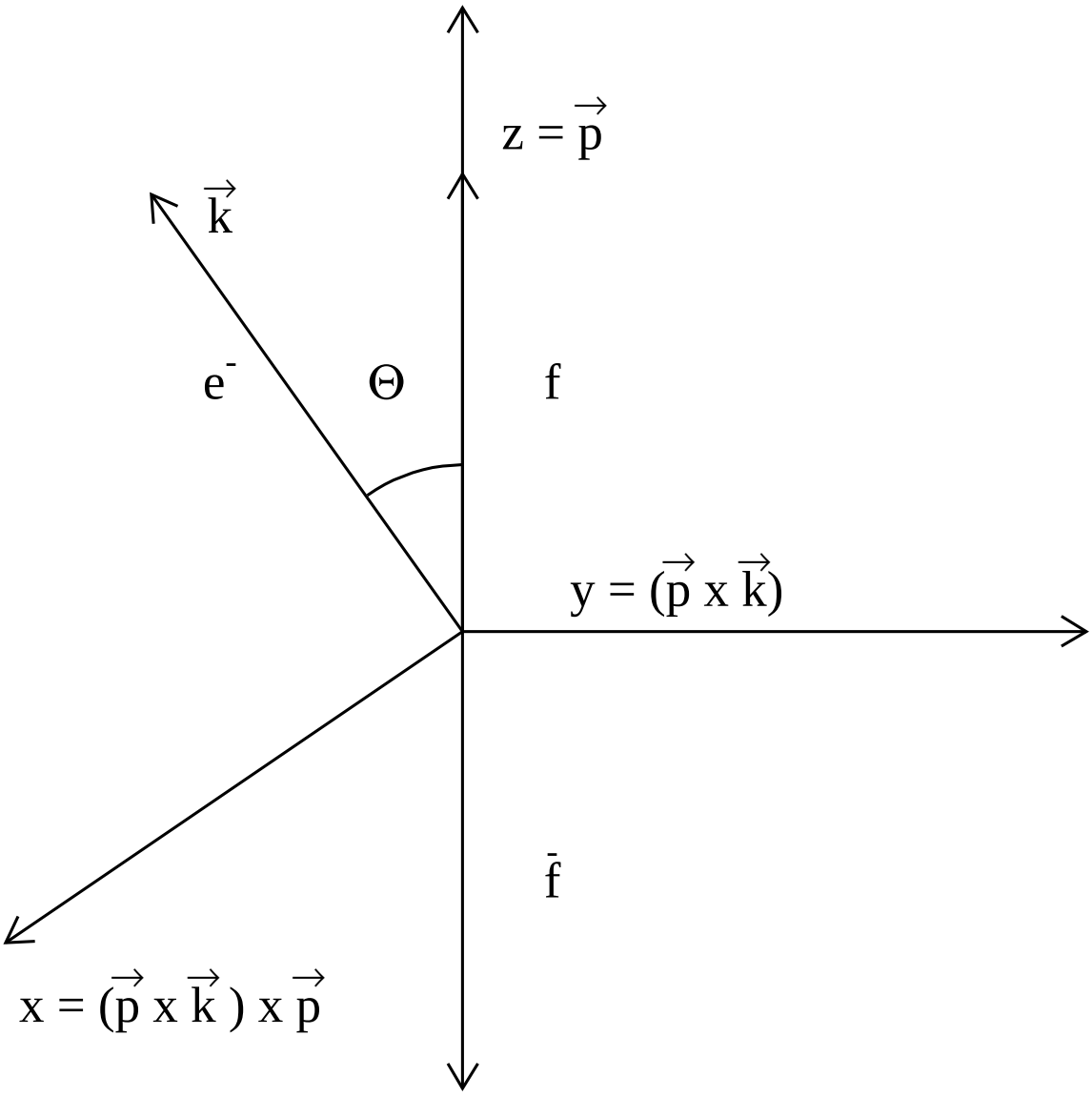

Figure 2.1: Coordinate system in the lab frame. $\vec{p}$ is the direction of the $\tau^{\pm}$. $\vec{k}^-$ is the direction of the incident e^-.

$$\begin{aligned}\frac{d\sigma}{d\Omega}(s_1^*, s_2^*) &= \frac{1}{16s}\{(1 + s_{1z}^* s_{2z}^*)[F_0(s)(1+\cos^2\theta) + F_1(s)2\cos\theta] \\ &- (s_{1z}^* + s_{2z}^*)[G_0(s)(1+\cos^2\theta) + G_1(s)2\cos\theta] \\ &+ [(s_{1y}^* s_{2y}^* - s_{1x}^* s_{2x}^*)F_2(s) + (s_{1y}^* s_{2x}^* + s_{1x}^* s_{2y}^*)G_2(s)]\sin^2\theta\} \quad (2.22)\end{aligned}$$

The form factors $F_i(s)$ and $G_i(s)$ contain the dynamic information of the theory. They are functions of the $fermion-Z^0$ and $fermion-\gamma$ coupling constants. These form factors are shown in Table 2.3, where we have defined:

$$P_0(s) = \frac{\alpha}{4\sin^2\theta_W \cos^2\theta_W}\; s\; \chi_0(s)$$

$$\begin{aligned}C_0 &= (|v_e|^2 + |a_e|^2)(|v_f|^2 + |a_f|^2) \\ C_1 &= 4\Re(v_e a_e^*)\,\Re(v_f a_f^*) \\ C_2 &= (|v_e|^2 + |a_e|^2)(|a_f|^2 - |v_f|^2)\end{aligned} \quad (2.23)$$

$$\begin{aligned}D_0 &= (|v_e|^2 + |a_e|^2)2\Re(v_f a_f^*) \\ D_1 &= 2\Re(v_e a_e^*)(|v_f|^2 + |a_f|^2) \\ D_2 &= -2\Im(v_f a_f^*)(|v_f|^2 + |a_f|^2)\end{aligned} \quad (2.24)$$

2.4 Polarization and Spin Correlation Observables

The different coefficients (2.23,2.24) of the cross section can be inferred by measuring certain asymmetries (namely the charge and polarization asymmetries defined bellow) as well as the transverse spin correlation between the leptons of the final state.

The *forward-backward* charge asymmetry (or simply, *forward-backward* asymmetry) is defined by,

$$A_{FB}^f = \frac{\sigma(cos(\theta) > 0) - \sigma(cos(\theta) < 0)}{\sigma} \quad (2.25)$$

Form factors	γ	γZ	Z
$F_0(s)$	$Q_f^2\alpha^2$	$-2Q_f\alpha\Re(v_e v_f)\Re P_0(s)$	$C_0\|P_0(s)\|^2$
$F_1(s)$		$-2Q_f\alpha\Re(a_e a_f)\Re P_0(s)$	$C_1\|P_0(s)\|^2$
$F_2(s)$	$-Q_f^2\alpha^2$	$2Q_f\alpha\Re(v_e v_f)\Re P_0(s)$	$C_2\|P_0(s)\|^2$
$G_0(s)$		$-2Q_f\alpha\Re(v_e a_f)\Re P_0(s)$	$D_0\|P_0(s)\|^2$
$G_1(s)$		$-2Q_f\alpha\Re(a_e v_f)\Re P_0(s)$	$D_1\|P_0(s)\|^2$
$G_2(s)$		$-2Q_f\alpha\Re(v_e a_f)\Im P_0(s)$	$D_2\|P_0(s)\|^2$

Table 2.2: Contribution to the $F_i(s)$ and $G_i(s)$ form factors from the photon and Z^0 exchange, and the $\gamma - Z^0$ interference

This asymmetry is a charge conjugation violation observable which does not depend on the spin of the final state leptons. This asymmetry can be obtained by integrating the formula 2.22 for all the final state spins, and can be expressed as a function of the basic parameters of the theory,

$$A^f_{FB}(s) = \frac{3}{4}\frac{F_1(s)}{F_0(s)}; \quad A^f_{FB}(M_Z^2) \approx \frac{3}{4}\frac{C_1}{C_0} \tag{2.26}$$

The *longitudinal* polarization of each of the final state τ's, for example of the τ^- (indeed, of each charged fermion in the reaction $e^+e^- \to f\bar{f}$), P_τ is defined as the number of τ^- with helicity $+1$ (that is $s^*_{1z} = 1$), minus the number of τ^- with helicity -1 ($s^*_{1z} = -1$), normalized to the total number of τ's. It can be obtained from formula 2.22 by requiring those values of s^*_{1z}, and it depends on the polar angle θ of the τ,

$$P_\tau(cos(\theta)) = -\frac{G_0(s)(1+\cos^2\theta) + G_1(s)2\cos\theta}{F_0(s)(1+\cos^2\theta) + F_1(s)2\cos\theta} \tag{2.27}$$

Due to the helicity conservation, the helicities of both τ's are completely correlated and the longitudinal polarization of the τ^+ and τ^- are identical. Physically the longitudinal polarization arises from parity violation in the Z^0 production and decay, and thus it is a parity violation observable. Neglecting the γ-exchange contribution one has

$$P_f(cos(\theta)) = -\frac{G_0(s)(1+\cos^2\theta) + G_1(s)2\cos\theta}{F_0(s)(1+\cos^2\theta) + F_1(s)2\cos\theta} \tag{2.28}$$

where neglecting the γ contribution:

$$P_f(cos(\theta)) = -\frac{P_f(1+\cos^2\theta) + 2P_Z\cos\theta}{(1+\cos^2\theta + 2P_Z P_f\cos\theta} \tag{2.29}$$

where

$$P_f = -\frac{D_0}{C_0} = -\frac{2\Re(v_f a_f^*)}{|v_f|^2 + |a_f|^2}$$

is the fermion polarization (averaged for all polar angles), and

$$P_Z = -\frac{D_1}{C_0} = -\frac{2\Re(v_e a_e^*)}{|v_e|^2 + |a_e|^2} \tag{2.30}$$

is the Z^0 polarization (which arises from parity violation at the $e^+e^- - Z^0$ vertex).

Neglecting the photon interference, the forward-backward asymmetry can be expressed in terms of P_Z and P_f as

$$A_{FB} = \frac{3}{4} P_Z P_f. \tag{2.31}$$

The remaining coefficients C_2 and D_2 can be measured through the correlation between the transverse spin components of the final state leptons. The expected value of the normal and transverse correlations coincide except for a global sign:

$$< P_T P_T > = - < P_N P_N > = \frac{F_2(s) \sin^2\theta}{1 + P_Z P_f 2\cos\theta/(1+\cos^2\theta)} \tag{2.32}$$

which can be expressed at the Z^0 peak as:

$$< P_T P_T > = \frac{A_{TT} \sin^2\theta/(1+\cos^2\theta)}{1 + P_Z P_f 2\cos\theta/(1+\cos^2\theta)} \tag{2.33}$$

where

$$A_{TT} = \frac{C_2}{C_0} \tag{2.34}$$

The A_{TT} is the only purely "weak" observable that breaks the symmetry between the vector and axial vector couplings shown by the observables P_Z and P_f. Traditionally, the predominance of the axial component predicted by the theory had been measured using the $\gamma - Z^0$ interference in the e^+e^- collisions.

The correlation between the normal spin component of the final state lepton f and the transverse spin component of the final state lepton $\bar{f}$ is the only non-zero T-parity odd observable in the Standard Model in the vanishing electron mass approach. The correlation is defined as:

$$< P_N P_T > \;=\; < P_T P_N >= \frac{A_{TN} \sin^2\theta/(1+\cos^2\theta)}{(1 + P_Z P_f 2\cos\theta/(1+\cos^2\theta)} \tag{2.35}$$

where

$$A_{TN} \;=\; \frac{D_2}{C_0} \tag{2.36}$$

The T-odd components of the cross section are related to CP violation terms or to absorptive terms generated by radiative corrections. In the frame of the Standard Model, the $< P_N P_T >$ term has another non-negligible contribution from the $\gamma - Z^0$ interference:

$$A_{TN} \;=\; \frac{D_2}{C_0} + \frac{2Q_f s_W^2 c_W^2 4 v_e a_f \Gamma_Z / M_Z}{C_0} \tag{2.37}$$

In the assumption of imaginary parts in the axial vector and vector couplings, P_Z and A_{TN} can been expressed as a function of the relative phase between both couplings:

$$\begin{aligned} D_2 &= -2\Im(v_f a_f^*) = -2|v_f||a_f|\sin(\Phi_{v_f} - \Phi_{a_f}) \\ D_0 &= 2\Re(v_f a_f^*) = 2|v_f||a_f|\cos(\Phi_{v_f} - \Phi_{a_f}) \\ \tan(\Phi_{v_f} - \Phi_{a_f}) &= \frac{D_2}{-D_0} = \frac{A_{TN}}{P_f} \end{aligned} \tag{2.38}$$

where the phases ϕ are defined by

$$\begin{aligned} a_f &= |a_f| e^{i\Phi_{a_f}} \\ v_f &= |v_f| e^{i\Phi_{v_f}} \end{aligned} \tag{2.39}$$

2.5 Correlated Decay Distributions

The spin components of the final state fermions cannot realistically be measured directly, the τ leptons produced at LEP decay close to the production point, before

reaching the detectors. This peculiarity is used to measure the polarization and spin correlation observables following the technique that was first proposed by Tsai [10], in which use is made of the angular and momentum distributions of the τ decay products. The experimental limitation of the measurement is that the τ direction cannot be reconstructed with efficiency and precision, so it is necessary to use experimental observables independent of the τ direction.

The correlated distribution of the τ decay products has been proved to be interesting to measure the τ longitudinal polarization [1, 2, 3, 4, 8] and the τ Michel parameters [9]. A similar method to measure the transverse and normal spin correlation has been proposed elsewhere [5, 7, 12, 14].

2.5.1 Tau decay

The decay distribution in the τ rest frame may be written in a general form as [13]:

$$d\Gamma^{\pm}(\vec{s}^*, \vec{q}^*) = \Gamma(\tau \to \nu_\tau X_i ...)[A_1^{(i)} \mp \alpha_i \vec{q}_i^* \vec{s}^* A_2^{(i)}] d^3 q_i^* \tag{2.40}$$

where $\vec{s}^*$ is the τ spin vector and $\vec{q}^*$ is the τ decay product momentum, both in the τ rest frame. The decay distribution functions $A_1^{(i)}$ and $A_2^{(i)}$ and the polarization parameter α_i depend on the particular decay channel.

Leptonic decay

The purely leptonic decay distribution is given in the SM by

$$A_1^{(i)} = \frac{1}{4\pi\lambda_i E_i^*}(-\frac{1}{6}m_i + \frac{1}{2}W_i E_i^* - \frac{1}{3}E_i^{*2})$$

$$A_2^{(i)} = \frac{1}{4\pi\lambda_i E_i^*}(W_i + \frac{P_i}{2} + E_i^*) \tag{2.41}$$

$$\alpha_i = -\frac{1}{3} \tag{2.42}$$

where W_i and P_i are the maximal energy and momentum of the leptons in the τ rest frame:

$$W_i = \frac{m_\tau^2 + m_i^2}{2m_\tau}, \quad P_i = \frac{m_\tau^2 - m_i^2}{2m_\tau} \tag{2.43}$$

where m_i is the lepton mass, and E_i^* the energy of the lepton in the τ rest frame.

The normalization factor turns out to be:

$$\begin{aligned}\lambda_i &= \int_0^{P_i} \frac{-\frac{1}{6}m_i + \frac{1}{2}W_i E_i^* - \frac{1}{3}E_i^{*2}}{E_i^*} q_i^{*2} dq_i^* = \\ &= \frac{1}{12}P_i^3 W_i - \frac{1}{8}m_i^2 P_i W_i + \frac{1}{8}m_i^4 \ln\frac{m_\tau}{m_i} \end{aligned} \tag{2.44}$$

Hadronic decay

For the hadronic processes the decay distribution functions turn out to be within the frame of the SM theory,

$$A_1^{(i)} = P_i A_2^{(i)} = \frac{1}{4\pi}\frac{\delta(q_i^* - P_i)}{P_i^2} \tag{2.45}$$

The polarization analyzer for the two-body decay processes ($x_i = \pi, \rho, a_1$) are:

$$\alpha_\pi = 1 \tag{2.46}$$

for scalar particles, and

$$\alpha_i = \frac{m_\tau^2 - 2m_i^2}{m_\tau^2 + 2m_i^2} (i = \rho, a_1) \tag{2.47}$$

for vector particles. The polarization analyzer are estimated to be $\alpha_\rho \approx 0.46$ and $\alpha_{a_1} \approx 0.12$ using the nominal values published in [16].

2.5.2 The process $e^-e^+ \to \tau^-\tau^+ \to x_1^- x_2^+ ...$

The combined process of $\tau^-\tau^+$ production and decay is given by the expression:

$$d\sigma(e^-e^+ \to x_1^- x_2^+) = 4d\sigma(\vec{s}_1^*, \vec{s}_2^*)\frac{d\Gamma_{x_1}(\vec{s}_1^*, \vec{q}_1^*)}{\Gamma_\tau}\frac{d\Gamma_{x_2}(\vec{s}_2^*, \vec{q}_2^*)}{\Gamma_\tau} \tag{2.48}$$

In the assumption of $\Gamma_\tau << m_\tau$, the cross section turns out to be:

$$4d\sigma(\vec{n}_1^*, \vec{n}_2^*)d\Gamma_{x_1}(\vec{s}_1^*, \vec{q}_1^*)d\Gamma_{x_2}(\vec{s}_2^*, \vec{q}_2^*) \tag{2.49}$$

where :

$$\begin{aligned}\vec{n}_1^* &= \alpha_1 \frac{A_2^{(1)}}{A_1^{(1)}}\vec{q}_1^* \\ \vec{n}_2^* &= \alpha_2 \frac{A_2^{(2)}}{A_1^{(2)}}\vec{q}_2^* \end{aligned} \tag{2.50}$$

Substituting expressions (2.50) into equation (2.22), the correlated distribution as a function of the τ rest frame observables is obtained:

$$\begin{aligned}\frac{d^8\sigma}{d\Omega d^3q_1^* d^3q_2^*} &= K(s)\left[A_1^{(1)}A_1^{(2)} + \alpha_1\alpha_2 A_2^{(1)}A_2^{(2)} q_1^* q_2^* \cos\theta_1^* \cos\theta_2^*\right] \\ &\quad \left[F_0(s)(1+\cos^2\theta) + F_1(s)2\cos\theta\right] \\ &\quad - \left[\alpha_1 A_2^{(1)}A_1^{(2)} q_1^* \cos\theta_1^* + \alpha_2 A_1^{(1)}A_2^{(2)} q_2^* \cos\theta_2^*\right] \\ &\quad \left[G_0(s)(1+\cos^2\theta) + G_1(s)2\cos\theta\right] \\ &\quad + \alpha_1\alpha_2 A_2^{(1)}A_2^{(2)} q_1^* q_2^* \sin\theta_1^* \sin\theta_2^* \sin^2\theta \\ &\quad [F_2(s)\cos(\phi_2^* - \phi_1^*) + G_2(s)\sin(\phi_2^* - \phi_1^*)] \end{aligned} \tag{2.51}$$

with

$$K(s) = \frac{1}{4s} \tag{2.52}$$

where q_i^*, θ_i^* and ϕ_i^* are the momentum, the polar and the azimuthal angles of the particle x_i in their corresponding τ_i rest frames.

The boost connecting the $\tau^\pm$ rest frame and the laboratory frame is defined by the parameters $\gamma = M_Z/(2m_\tau)$, and $\beta = \sqrt{1-\gamma^{-2}}$. The variables in both frames are related by:

$$\begin{aligned} E_i^* &= \gamma(E_i - \beta q_i \cos\theta_i) \\ q_i^* \cos\theta_i^* &= \gamma(q_i \cos\theta_i - \beta E_i) \\ q_i^* \sin\theta_i^* &= q_i \sin\theta_i \\ \phi_i^* &= \phi_i \end{aligned} \tag{2.53}$$

with the Jacobian

$$\frac{\partial(q_i^*, \cos\theta_i^*)}{\partial(q_i, \cos\theta_i)} = \frac{E_i^*}{q_i^{*2}}\frac{q_i^2}{E_i} \tag{2.54}$$

The range of the angular variables depends on each decay channel. For the one-prong hadronic decays the angle θ_i is fixed, since it is related to the energy E_i and is given by

$$\cos\chi_1 = \left(\frac{\gamma E_i - W_i}{\beta\gamma q_i}\right) \tag{2.55}$$

For the leptonic decays, the angle in the laboratory frame, θ_i, varies in the range $0 \leq \theta_1 \leq \chi_i$, where χ_i is as defined above.

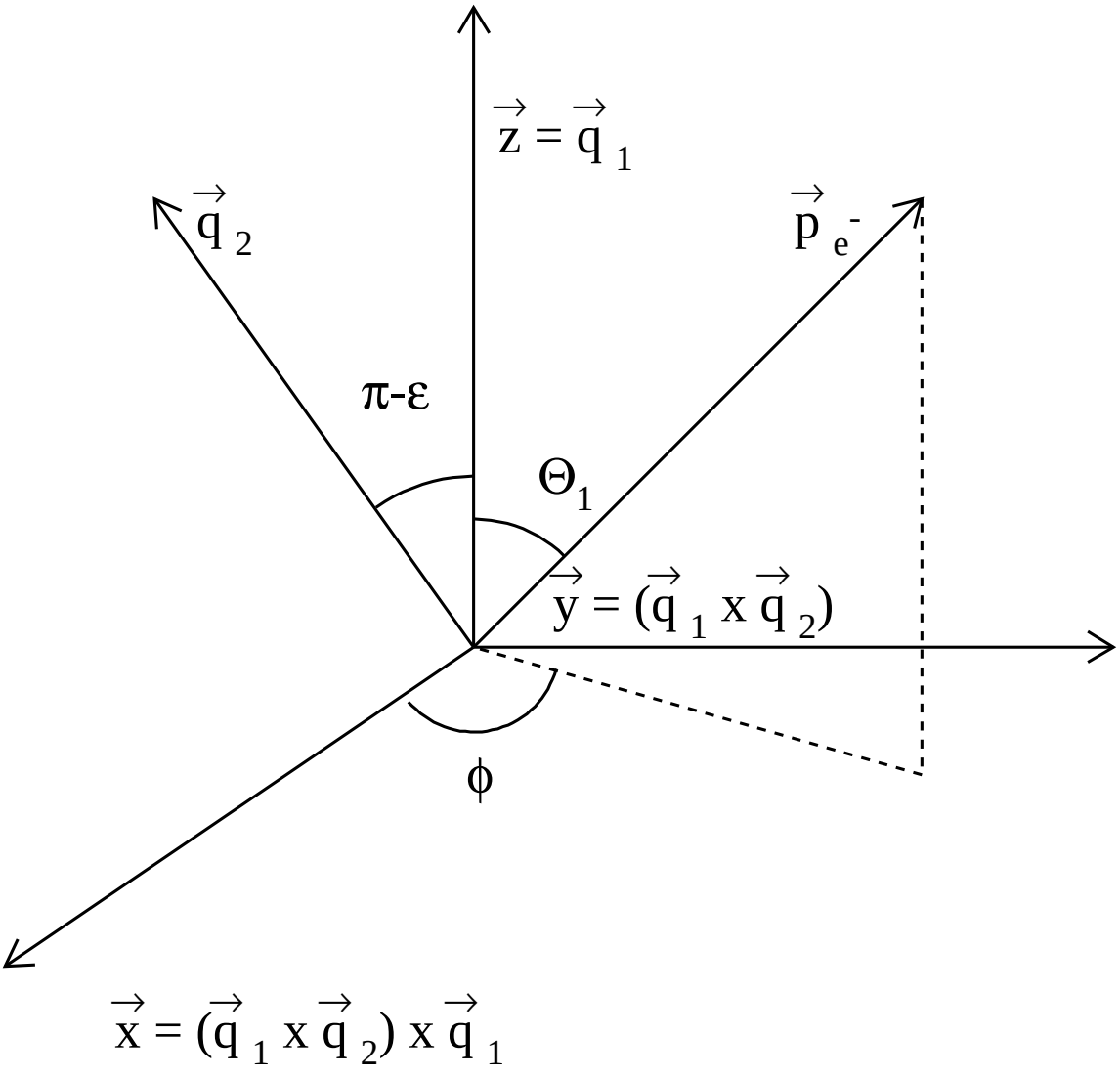

Figure 2.2: Coordinate system in the lab frame. $\vec{q_1}$ ($\vec{q_2}$) is the direction of the τ^- (τ^+) decay product. $\vec{p}_{e^-}$ is the direction of the incident e^-.

The resulting distribution depends on the τ direction (θ) in the laboratory frame. Without the experimental reconstruction of the τ direction, one cannot measure these quantities. The aim here is to analyze the resulting correlations when the τ direction is integrated out in (2.51). For this purpose the laboratory frame is defined as indicated in Fig.2.2. In this frame the τ decay products momenta

are given by:

$$\begin{aligned} \vec{q_1} &= q_1(0,0,1) \\ \vec{q_2} &= q_2(\sin\epsilon, 0, \cos\epsilon) \end{aligned} \tag{2.56}$$

and the $\tau^{\pm}$ and electron beam momenta:

$$\begin{aligned} \vec{p}_{e^-} &= (\sin\theta_1\cos\phi, \sin\theta_1\sin\phi, \cos\theta_1) \\ \vec{p}_{\tau^-} &= (\sin\chi_1\cos\Phi_1, \sin\chi_1\sin\Phi_1, \cos\chi_1) \\ \vec{p}_{\tau^+} &= -\vec{p}_{\tau^-} \end{aligned} \tag{2.57}$$

The angles in (2.51) (the angle θ between the e^- and the τ^-, the angle θ_2 between the τ^+ and its decay product, and the angle θ_+ between e^- and the τ^+ decay product) can be expressed as a function of the new variables:

$$\begin{aligned} \cos\theta &= \cos\theta_1\cos\theta_- + \sin\theta_1\sin\theta_-\cos(\Psi-\phi) \\ \cos\theta_2 &= \cos\theta_1\cos\epsilon - \sin\theta_1\sin\epsilon\cos(\Psi) \\ \cos\theta_+ &= -\cos\theta_-\cos\epsilon + \sin\theta_-\sin\epsilon\cos(\phi) \end{aligned} \tag{2.58}$$

The angles χ_1 and ϵ can be expanded to the dominant order in the dilation factor γ^{-1}, taking into account that due to the boost, one has $\chi_1 \approx \gamma^{-1}$ and $\epsilon \approx \gamma^{-1}$. After the integration of the τ direction (χ_1,Φ_1) the cross-section can be written as a function of the experimental angles (ϵ,θ_1,ϕ) [7]:

$$\begin{aligned} \frac{d^3\sigma}{d\Omega_- d\epsilon} &= K(s)[R_0(\epsilon)(1+\cos^2(\theta_1)) + \\ &\quad R_1(\epsilon)2\cos(\theta_1) + R_2(\epsilon,\phi)\sin^2(\theta_1)] \end{aligned} \tag{2.59}$$

with

$$\begin{aligned} R_i(\epsilon) &= F_i(s)Q_1(\epsilon) + G_i(s)Q_2(\epsilon)(i=1,2) \\ R_2(\epsilon) &= Q_3(\epsilon)\left[F_2(s)\cos(2.\phi) + G_2(s)\sin(2.\phi)\right] \end{aligned} \tag{2.60}$$

The $Q_i(\epsilon)$ depend on the specific τ decay considered. The nature of the decay and its spin enter in the polarization parameter α_i (see appendix B for more detailed description), which is a multiplicative factor contained in $Q_i(\epsilon)$, while the mass of the particle affect the shape of the $Q_i(\epsilon)$. Continued in Appendix A is a description of how to calculate the $Q_i(\epsilon)$ numerically, which has been published [17].

Chapter 3

The ALEPH detector

3.1 The LEP storage ring

The LEP (Large Electron Positron) storage ring, approved in 1981, is a e^+e^- collider located at CERN (European Laboratory for Particle Physics). The project was conceived like a precision machine to perform detailed measurements of the Z^0 and $W^\pm$ bosons, and searching for phenomena beyond the Standard Model.

The LEP project consists in two stages. Up to the end of 1995 LEP was running at the center of mass energy equal to the Z^0 mass ($M_{Z^0} \approx 91.18$ GeV/c^2), at this energy the event production is dominated by the Z^0 resonance. A second stage, starting from spring 1996, is planning to reach up to 200 GeV in the center of mass, enough to produce pairs of $W^\pm$ bosons.

LEP is situated in a circular tunnel of 8.5 km diameter, whose depth varies from 50 to 150 m. The LEP ring consists of eight arcs alternating with eight straight sections. The four experiments, L3, DELPHI, OPAL, and ALEPH, are positioned in the straight sections where the electron and the positron bunches collide.

The electromagnetic guide field system of LEP consists of dipoles, quadrupoles, sextupoles, horizontal and vertical dipole corrector, rotated quadrupoles, and electrostatic dipole deflector. The electrons and the positrons are bended by the dipole magnets. The alternation of quadrupoles rotated 90 degrees along the beam axis produce a strong focusing effect to increase the machine luminosity. The sextupoles are used to compensate the dependence of the focusing effect on the beam energy ("chromaticity").

The acceleration system consist in 128 five-cell copper cavities. The operative frequency is 352.21 MHz, which corresponds to 31,320 times the revolution frequency of a beam circulating in LEP, that means a total of 31,320 buckets for LEP, with the possibility of stable oscillations in each. However in order to collide the e^-e^+ in the center of the detectors only some of those buckets are injected and accumulated. The LEP bunch configuration has been changing in order to improve the beam intensity and, consequently, the luminosity. The first LEP configuration consisted in 4 bunches of electrons and positrons, separated by $\approx 23.0\mu$s. From October 1992 up to 1994 LEP was running with a 8x8 bunches configuration, separated by $\approx 12.5\mu$s. During 1995, LEP went back to the 4x4 bunch configuration but each bunch was divided into two. This is the proposed configuration to achieve high luminosity performance for 200 GeV LEP.

The LEP storage ring is the last accelerator in a chain of five (figure 3.1). The electrons are accelerated in a linac up to 200 MeV. A fraction of these electrons is used to create positrons colliding the electron beam with a fixed tungsten target. Both electron and positrons are accelerated to 600 MeV in a second linac. The beam is stored into a 600 MeV electron-proton accumulator (EPA), which inject into the CERN proton synchrotron (PS) operating at a 3.5 GeV. The PS then inject the beam into the CERN Super Proton Synchrotron (SPS), which operates as a 20 GeV electron-positron injector for LEP.

The location of the collider and its four experimental areas are shown in 3.2.

3.2 The ALEPH detector

ALEPH (Apparatus for LEP PHysics) is one of the four large experiments of the LEP storage ring. ALEPH is locate at the interaction point number four, in a cavern at 143 m underground. The approximated dimensions of the apparatus is $12 \times 12 \times 12\ m^3$, and a weight of around 4000 tons.

ALEPH, like the other three experiments at LEP, is devoted to measure the momentum, energy and identify the particles created in the e^+e^- collisions. ALEPH is a cylinder surrounding the interaction point and covering 95% of the solid angle around it. The apparatus is composed of independent and modular subdetectors devoted for specific tasks. The subdetectors are grouped into tracking devices and

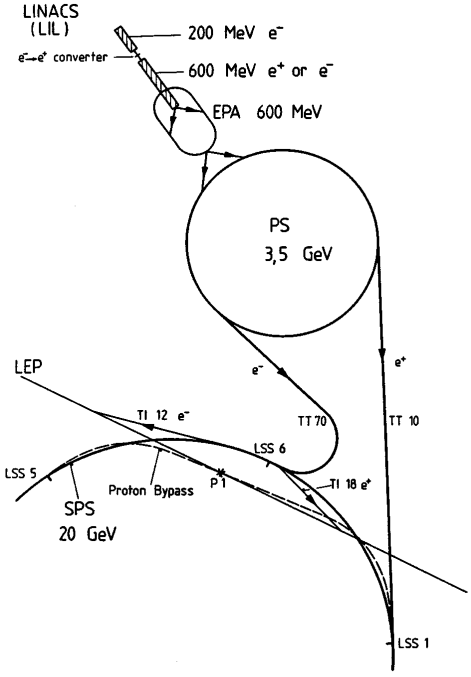

Figure 3.1: LEP acceleration chain.

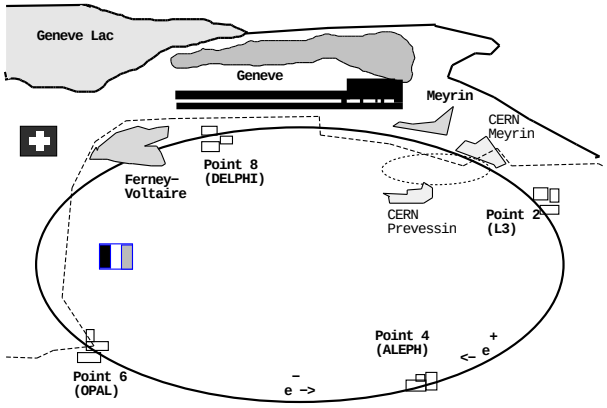

Figure 3.2: View of LEP and the location of the experimental areas.

calorimeters.

The tracking devices measure the direction and momentum of the charged particles. ALEPH tracking is performed by silicon and gas detectors. The conceptual principle of these subdetectors is the following: the charged particle ionize the media passing through, this charge is drifted by an electric field in the gas detectors to be measured in wires. The charged produced into the silicon is amplified and measure in the same silicon wafer which is segmented to obtain position information. All the tracking devices are embedded into a strong magnetic field (1.5 T) which curve the charged particles trajectories and allows to infer their momenta. Three different tracking detectors are installed in ALEPH, from the interaction point: the silicon microVertex DETector (VDET) [19], the multiwire Inner Tracking Chamber (ITC)[20] and the Time Projection Chamber (TPC) [21].

The calorimeters are devoted to measure the energy of the particles interacting with a dense material. Particles in the calorimeters interact with the material generating secondary particles that in turn interact with the material. This shower of particles generates a measurable signal proportional to the energy of the initial particle in some instrumented materials. There are two kind of calorimeters depending on the kind of particles that one wants to measure. The Electromagnetic CALorimeter (ECAL) is devoted to measure the energy of electrons and photons. The Hadronic CALorimeter (HCAL) is design to detect hadrons. The interaction of the electromagnetic particles (electrons and photons) with the matter is propagated through successive electron-positron pair creation, bremsstrahlung, photon radiation, compton scattering,.... The interaction of the hadrons with the matter is dominated by the strong interaction (QCD) and the secondary particles propagates through successive inelastic strong interaction.

The main components of the ALEPH detector are shown in 3.3.

The measurement of the luminosity is basic for some electroweak measurements. Three devices have been installed in the ALEPH detector to measure accurately such a quantity. The luminosity is measured through the computation of the rate of a well known process (Bhabha) and dividing the observed rate by the theoretical cross-section. The three subdetectors installed in ALEPH cover different angular ranges,

- LCAL (Luminosity CALorimeters) covering the angular range from θ =

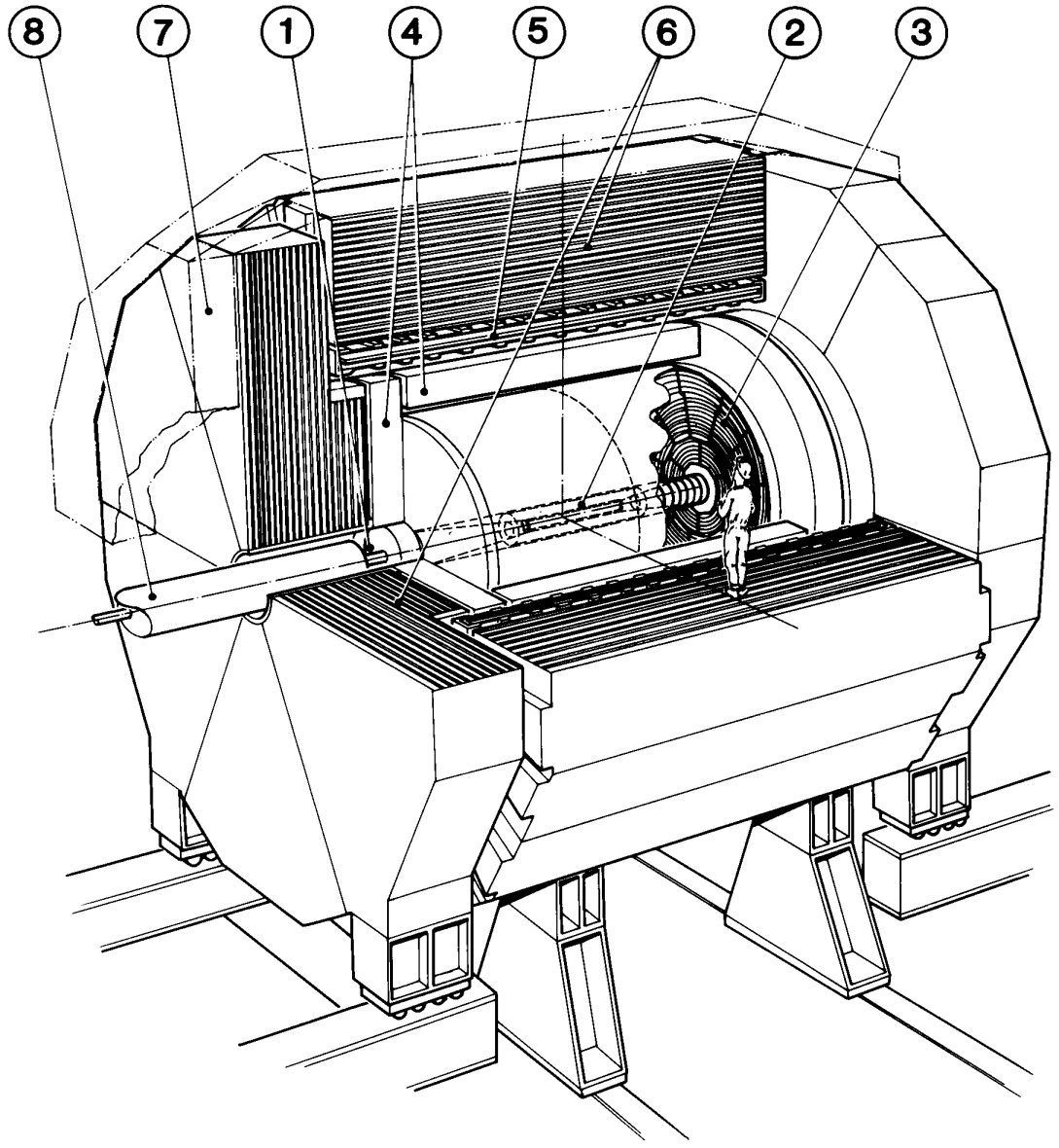

Figure 3.3: Schematic view of the ALEPH detector. (1) Luminosity Monitor. (2) Inner Tracking Chamber. (3) Time Projection Chamber. (4) Electromagnetic Calorimeter. (5) Superconducting Coil. (6) Hadronic Calorimeter. (7) Muon Chambers. (8) Beam Pipe.

38.4 mrad to $\theta = 195$ mrad,

- SICAL (Silicon luminosity CALorimeters) [22] covers the angular range from $\theta = 27.9$ mrad to $\theta = 62.7$ mrad,

- BCAL [23] is a very small angle calorimeter sited at 7.7 m of the interaction point behind the final focusing quadrupole covering the angular range from $\theta = 5.1$ mrad to $\theta = 9$ mrad.

The two first measure the luminosity with high precision ($\approx 0.1\%$) and the third one gives an on-line luminosity.

Other devices are installed in the ALEPH detector to monitor the radiation and the beam background (SAMBA), and the beam position (BOMB).

In the following we will describe in more detail the subdetectors which are most relevant for the present analysis, VDET, ITC, TPC, ECAL, HCAL and the muon chambers.

3.2.1 VDET

The microVertex DETector (VDET) consists on two concentric double-side layers of silicon wafers, surrounding the beam pipe. The inner wafer is located at a radius of 6.3 cm and the outer at 11.0 cm. The readout strips are on both sides of the silicon wafers, parallel and normal to the beam direction. For normal incident track the point resolution is $\sigma_{r\phi} \approx 12\mu m$ and $\sigma_z \approx 10\mu m$.

VDET has two main features. One of them allows to reconstruct the decay vertex of short life particles (like beauty mesons or τ leptons) to measure its lifetime and to separate these particles from those produced at the primary interaction point. Another feature is to improve the precision in the reconstruction of charged tracks. VDET hits are selected extrapolating track found by the ITC and TPC to the VDET layer. The track is refitted including those hits achieving at 45 GeV a momentum resolution

$$\frac{\Delta p}{p^2} = 6.10^{-4}(\mathrm{GeV/c})^{-1}$$

3.2.2 ITC

The Inner Tracking Chamber (ITC) is a cylindrical multiwire drift chamber. The cylinder is 2 m long, the inner radius is 12.8 cm and the external radius is 28.8 cm. The chamber is filled with a gas mixture composed by $Ar(50\%)$ and $C_2H_6(50\%)$. The sense wires made of tungsten and gold are distributed in a set of 8 concentric layers, the diameter of each wire is 30 μm and they are all located parallel to the beam direction. The acceptance for particle passing through the 8 wire layers is between 14 and 165 degrees.

The ITC has two main purposes in ALEPH, the first one is to provide tracking information to the "Level 1 of trigger" 2-3 μs after the collision. The second purpose is to provide up to 8 coordinates for charged particles. The $(r-\phi)$ coordinate is obtained measuring the drift velocity of the electrons produced in the ionization. The z coordinate is obtained by measuring the time difference between the electric pulses at the end of the sense wires. The ITC tracking precision is measured to be about 150 μm in the $(r-\phi)$ plane and about 5 cm for the z coordinate. The momentum resolution at 45 GeV including the ITC and the TPC information is

$$\frac{\Delta p}{p^2} = 8.10^{-4}(\mathrm{GeV/c})^{-1}$$

3.2.3 TPC

The Time Projection Chamber (TPC) is the main tracking detector of ALEPH. The chamber has a cylindrical structure of 4.7 m long with 35 cm and 180 cm of inner and outer radius respectively (figure 3.4). The TPC is filled with 43 m^3 of a nonflammable gas mixture of Ar(91%) and $CH_4(9\%)$ at atmospheric pressure. The electric drift field (110 V/cm) extends in the z direction from each end-plate towards the central membrane that divides the chamber into two halves.

The electrons produced by ionization of transversing charged particles drift towards one end-plate following the electric drift field. At the end-plates they induce ionization showers in a plane of wire chambers. There are 18 of these wire chambers called sectors on each end-plate. The detection of these showers provides information about the impact point and the arrival time of the drifting electrons. Each sector consists on three layers of wires (figure 3.5):

- The gating grid prevents positive ions produced in the avalanches near the sense wire from entering the main TPC volume and distorting the electric field.
- The cathode wires keep the end-plates at null potential and together with the central membrane create the electric field.
- The sense wires are read out to give the energy deposition and the z measurement of the tracks. The dE/dx is then obtained dividing the collected charged by the length of the reconstructed trajectory of the particle. The dE/dx value is very useful for particle identification: $e^{\pm}, \mu^{\pm}/\pi^{\pm}, K^{\pm}, p, ...$ mainly for low momenta particles.

The TPC measures the trajectory of the particles in three dimensions. The z direction is obtained through the measurement of the drift time. The ϕ coordinate is calculated interpolating the signals induced on cathode pads located precisely on the sectors. The radial coordinate is given by the radial position of the pads involved in the measurement. The TPC provides up to 21 3-dimensional points of each charged track crossing the chamber.

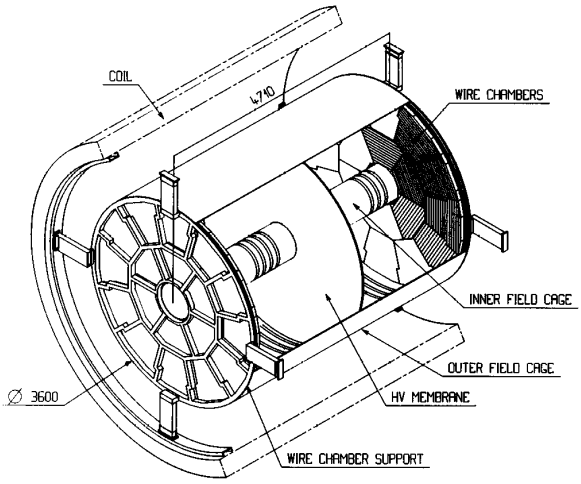

Figure 3.4: View of the TPC.

The error in the coordinates measurement depends on various factors. The error in the z coordinate is mainly due to the diffusion of the electrons as they drift

to the end-plates. In the $r-\phi$ components, the error depends on the values of the angles of the tracks with respect to the sensing wires and to the cathodes.

The helicoïdal trajectory of the particles can be fitted to the 3-d points. The projection on the end cap plate is an arc of circle which radius of curvature is proportional to the modulus of the momentum component which is perpendicular to the magnetic field. The momentum resolution using the TPC information is:

$$\frac{\Delta p}{p^2} = 12.10^{-4}(\mathrm{GeV/c})^{-1}$$

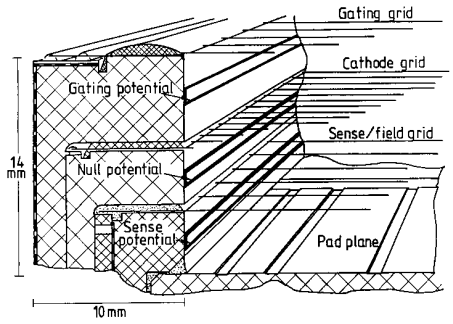

Figure 3.5: Edge of the TPC.

3.2.4 ECAL

The ALEPH electromagnetic calorimeter (ECAL) is a sampling calorimeter made of lead sheets and proportional gas chambers. This calorimeter has been designed to measure the energy and the impact position of electromagnetic showers with large hermeticity (3.9 π sr with cracks representing 2% of the barrel and 6% of the end-caps). The ECAL detector is arrange as a barrel surrounding the TPC, closing at both ends with end-caps (figure 3.6). The barrel and end-cap are divided in modules sustaining 30^o in the azimuthal angle. The end-caps and the barrel are rotated 15^o to each other, and, in order to avoid the overlapping of the calorimeter crack regions. The ECAL subdetector is rotated -1.875^o with respect of the hadron calorimeter.

The barrel is organized in twelve modules made of 4096 (32×128) towers each. Each module is a sandwich of 45 lead and wire-chamber layers. The total thickness

is equivalent to 22 radiation lengths, X_0. The structure of every single layer has three different elements (figure 3.7),

- a lead sheet of 0.2 cm (0.5 radiation length) thickness,
- a wire plane (anode plane), which are made of aluminum extrusion,
- and a pad plane (cathode plane) covered by a graphite mylar sheet. The cathode pads are connected internally forming towers covering about $1^\circ \times 1^\circ$ regions of solid angle.

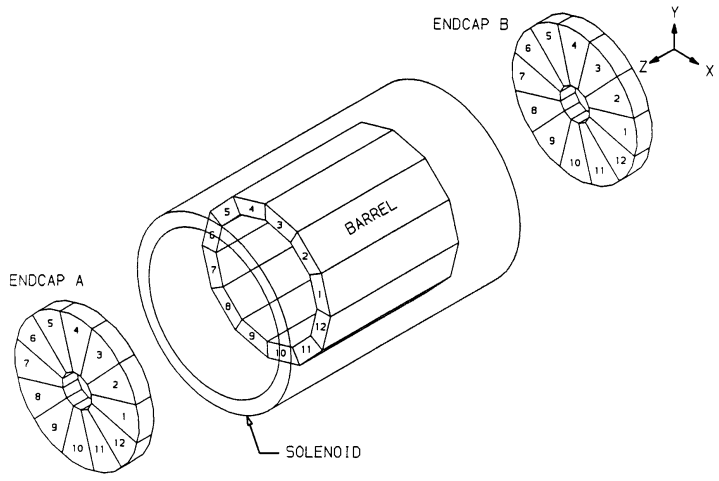

Figure 3.6: Overall geometry of the electromagnetic calorimeter.

The layers of consecutive layers are summed independently in three depths corresponding to:

- 1^{st} stack: 4 X_0 = 10 layers of 2mm lead sampling.
- 2^{nd} stack: 9 X_0 = 23 layers of 2mm lead sampling.
- 3^{rd} stack: 9 X_0 = 12 layers of 4mm lead sampling.

In addition to the analogue signals from each tower's storey, the analogue signal from the anode wire plane is used in the setting up, testing and calibration of the modules, in the trigger and for analysis.

The energy resolution is measured to be:

$$\frac{\sigma_E}{E} = \frac{.18\text{GeV}^{1/2}}{\sqrt{E}} \oplus 0.02, \tag{3.1}$$

and the position resolution is

$$\sigma_x = \sigma_y = \frac{6.8\text{mm GeV}^{1/2}}{\sqrt{E}} \tag{3.2}$$

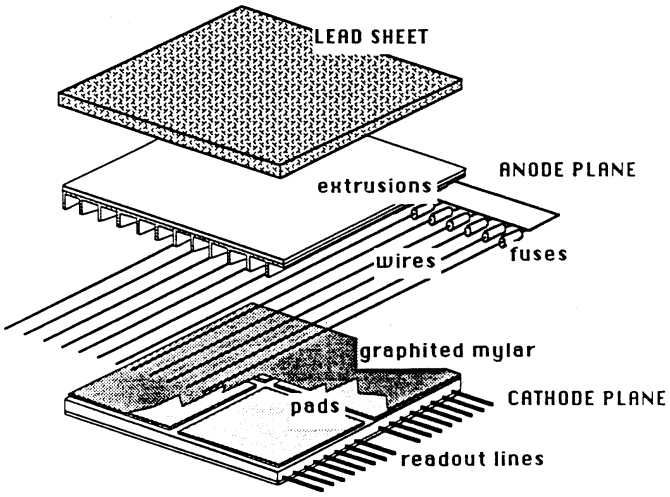

Figure 3.7: View of the ECAL stack layer.

3.2.5 HCAL and Muon Chambers.

The Hadronic Calorimeter (HCAL)[18] is a sampling calorimeter of streamer and iron sheets that constitutes the main support of the ALEPH subdetectors, collects the return flux of the magnetic field, but also acts as a hadron absorber. The calorimeter is composed of a barrel outside the superconducting coil and two end-caps. In the outer side of the iron two double layers of streamer tubes are provided to detect muons escaping the detector. The structure is shown at figure 3.8.

The Hadronic Calorimeter consists of 12 modules in the barrel plus 6 modules forming each end-cap. Each module is structured into 22 layers of iron, 5 cm thick, and a final one, 10 cm thick. The streamer tubes are inserted in the gaps between

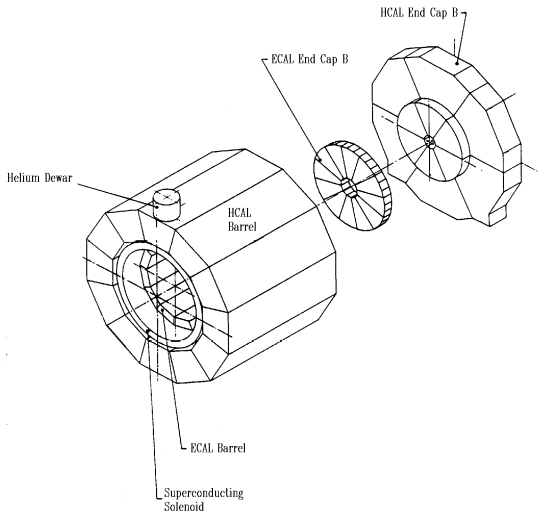

Figure 3.8: Overall geometry of the hadronic calorimeter.

the iron sheets. The total iron thickness is 1.2 m, equivalent to 7 interaction lengths. The streamer tubes consist of plastic (PVC) comb profiles having eight cells each. On both sides of the comb the pulses are induced onto external electrodes. On one side copper pads are placed and summed to build up to 4788 projective towers pointing to the interaction point. On the other side of the comb profile, aluminum strips follow each individual tube for its length. These pads provide a logical signal if the tube has been fired. Altogether the strips provide a two dimensional view of the hadronic signals and are very effective to identify muons. This digital readout is also use for the level-1 trigger.

The energy resolution of the hadronic calorimeter is given by the expression:

$$\frac{\sigma_E}{E} = \frac{(0.85 \pm 0.01)\mathrm{GeV}^{-1/2}}{\sqrt{E}}, \tag{3.3}$$

and the angular resolution is about 10 mrad for muons.

3.3 The trigger system

The high segmentation of the ALEPH detector (it has more than 500000 electronic channels) needs a large volume of information of the "raw data" to be recorded when and event is read. In order not to exceed the storage information capacity and decrease the dead time due to the detector readout some restrictions have to be applied to filter efficiently the background keeping the electron and positron collisions. The background is mainly due to the cosmic rays, the collision of electrons with the residual gas, the bremsstrahlung radiation photons and the off-momenta beam electrons hitting the beam walls. The "online" selection is made by the "trigger system". The trigger activates the readout process only when certain conditions are satisfied. The trigger was designed to take a decision between beam crossings, i.e. every 11 μs in the 8 bunch configuration. The data recording rate should be at the level 1-2 Hz.

The goal of the whole trigger system is to be sensitive to single particles and jets. To achieve these requirements the trigger system is organized in three different layers, the "lowest" level are hardware implemented to give a fast answer to accept or not the current event. The "highest" level are implemented by software.

The different trigger levels are:

- **LEVEL 1 (LVL1)**

  It is based on the ITC, ECAL and HCAL information. The LVL1 decision is taken 5 μs after the beam crossing, which allows to be ready for the next crossing in the LEP 8 bunch mode configuration. A positive answer from LVL1 initiates the digitization of the signals.

  The answer of this level is obtained based on different "physics triggers". One trigger involves coincidences between ITC tracks and energy deposited in ECAL, similar trigger is based on HCAL/ITC coincidences. Another trigger accounts for the energy deposited in ECAL. The luminosity trigger is based on the energy deposited in the LCAL modules. Other triggers are implemented for neutral electromagnetic and hadronic energy and for back-to-back hits in the ITC.

- **LEVEL 2 (LVL2)**

After passing the LVL1 trigger the LVL2 trigger checks that the trajectories of the charged particles in the TPC originate close to the interaction point. The decision is taken in 50 μs which is the time required for the drifting electron to arrive to the TPC end plates. The maximum trigger rate allowed for the level two is about 10 Hz. After a LVL2 YES the full detector readout is started.

- **LEVEL 3 (LVL3)**

  The LVL3 trigger is software implemented. It consist in a program that makes a bare reconstruction of the event, and verify the LVL1 and LVL2 decisions. The whole detector information is used to reduce the amount of data to be stored to an acceptable rate level ($\approx$ 500 Mb/s), but keeping all the interesting physic events.

3.4 Data Acquisition System and Event Reconstruction

The data acquisition system (DAQ) allows each subdetector to take data independently, process all the information taken by the detector, activates the trigger system at every beam crossing, writes data in a storage system and monitorizes and regulates continuously all the detector and electronic systems.

The DAQ architecture is highly hierarchical. The flow control from the beam crossing up to the storage device is described below:

- Timing, Trigger and Main Trigger Supervisor: synchronize the readout electronic to the beam crossing in the accelerator and inform the ReadOut Controllers (ROC) about the data viability.
- ROC's: initialize the front-end modules, read them out and format the data.
- Event Builders (EB's): build a subevent at each subdetector level and provide a "spy event" to a subdetector computer.
- Main Event Builder (MEB): collects the pieces of an event from the various EB's and ensures resynchronization and completeness.

- Level three trigger: performs a refined data reduction.
- Main host and subdetector computers: The main machine (an AXP Cluster) initializes the complete system, collects all data for storage and provides the common services. Tasks associated to each subdetector get the "spy events" and perform the monitoring of the subdetectors.

The data is taken by the online computers is called raw data. The raw data is reconstructed quasi online. In less than two hours after the data is taken, the event reconstruction and a check of the quality of the data is done, thus allowing ALEPH to have a fast cross-check of the data and to correct possible detector problems. This task is done by the Facility for ALeph COmputing and Networking (FALCON) [24].

Chapter 4

Selection of events

The $\tau^+\tau^-$ event selection consists on the identification of τ decay channels plus additional cuts aimed at increasing the purity of the sample. In order to increase the sensitivity to the transverse spin correlations, the analysis requires the identification of each τ decay channel, see Appendix B. The identification of τ decay product as a lepton ($e^\pm$ or $\mu^\pm$), a $\pi^\pm$ or a $\rho^\pm$, selects τ pair events with a small contamination from non-τ events. The remaining background from the $e^+e^- \to e^+e^-X$, $e^+e^- \to e^+e^-$, $e^+e^- \to \mu^+\mu^-$ and $e^+e^- \to q\bar{q}$ processes is reduced by applying specific cuts that are based on the kinematics of the $\tau^+\tau^-$ events.

The selection has three main steps. First, a preselection of the events is done, as described in section 4.1. Second, the leading track of each hemisphere is identified to be one of the particles, $e^\pm$, $\mu^\pm$ or $\pi^\pm$. The particle identification is described in section 4.2. The identification of π^0 from $\rho^\pm$ decays is explained in section 4.3. The final selection to reduce the remaining background is described in section 4.4.

4.1 Preselection

The preselection requirements are based on TPC tracks only. Only the tracks with more than 4 TPC hits, $|z_0| < 10$ cm[1], and $|p| > 0.1$GeV are considered. They are labeled as "good tracks" when there are two of these tracks with $|d_0| < 5$ cm[2]. For the events with 2 to 8 tracks a different procedure is followed: the tracks with

[1] z_0 is the z coordinate at the point of closest approach to the beam axis.
[2] d_0 is the distance of closest approach to the beam axis.

$|d_0|$ <2 cm are labeled as "good tracks", and any track with 2 cm< $|d_0|$ < 5 cm is declared a "bad track".

The events are required to pass the following criteria:

- there is at least one good track per hemisphere. The hemispheres are defined along the thrust axis which is computed from the good charged tracks,
- there are less than 8 good tracks per event,
- there is at least one track with $|d_0|$ <2 cm that has a momentum exceeding 3 GeV/c,
- if there are more than 4 good tracks, each of them is required to have an opening angle, η, with respect to the axis of the corresponding jet such that $\cos(\eta) > 0.85$.

With this preselection, most of the Z^0 decays to hadrons are excluded by the cuts requiring less than nine tracks coming from the interaction region, and the maximum opening angle of the charged particles with respect to the axis of the jet. The two-photon events are rejected requiring that one good track has a momentum above 3 GeV/c.

The main source of "bad tracks" is coming from photon conversions, nuclear interactions and cosmic rays. These tracks are included in the preselection to keep the tracks from photon conversions. The photon conversions, around 25% of the total sample, are needed to increase the efficiency in the ρ reconstruction.

The remaining events after this preselection are mainly e^+e^- events, $\mu^+\mu^-$ and $\tau^+\tau^-$ events with low multiplicity.

4.2 Charged Particle Identification

The identification of the tau decay channel plays an important role in the measurement of the transverse spin correlations as it is explained in Appendix B. To identify the particles a likelihood method is used incorporating the relevant information from the ALEPH detector, i.e., the electromagnetic and hadronic calorimeters. For that, a probability to be $\mu^\pm$, $\pi^\pm/K^\pm$ or a $e^\pm$ is associated to each "good track" in the event.

4.2.1 Likelihood identification method

A set of discriminating variables, x_i, is selected and the corresponding probability densities $f_i^j(x_i)$ for a particle j are computed using the ALEPH Monte Carlo Simulation. The method is explicitly described in [25]. The global probability estimator P_j is defined as

$$P_j = \frac{\prod_i f_i^j(x_i)}{\sum_j \prod_i f_i^j(x_i)} \tag{4.1}$$

where $j = e, \pi(K), \mu$. Each charged particle is assigned to the type with the largest global estimator P_j.

The discriminating variables are based on the the dE/dx in the TPC, two estimators of the shower profile in ECAL, three variables in HCAL, plus two variables measured in the Muon Chambers. The variables are explicitly:

- dE/dx, the energy loss in the TPC which separates e's from π's and μ's.
- R_T, which is the transverse shape of the energy deposition in ECAL.
- R_L, which is the inverse of the mean position of the energy deposition in three ECAL stacks.
- $\bar{W}$, or the averaged shower width in HCAL.
- N_{10}, the number of fired planes in the last ten HCAL planes.
- E_H, the energy measured with the HCAL pads.
- N_μ, which is the number of hits in the muon chambers with a road of $\pm 4\sigma$ around the track extrapolation, where σ is the standard deviation expected from multiple scattering.
- $\bar{D}_\mu$, the average distance (in units of multiple scattering standard deviation) of the hits from their expected position in the muon chambers.

The ECAL variables R_T and R_L are related to the transverse and longitudinal development of the shower in ECAL. The HCAL variables $\bar{W}$ and N_{10} are derived from the digital read-out of HCAL.

Some minimal cuts are necessary before a track is identified. Because of the range of μ in HCAL, a track can be identified only above 1.8 GeV/c, so a minimum momentum of 2 GeV/c is applied for muon and hadron candidates. A cut is applied around the ECAL cracks for electrons and hadrons. The inefficiencies from this bare cuts are known very precisely because they rely on the detector geometry and the momentum calibration.

By construction one has $\sum_j P_j = 1$ and, due to $e-\mu$ identification "orthogonality" in the detector, one of the relations holds: $P_\mu + P_h = 1$ or $P_e + P_h = 1$. Therefore the chosen particle has always P_j greater than 0.5.

4.3 π^0 Identification

The spectrum of π^0 in $\tau^+\tau-$ pairs goes from a few MeV to the nominal beam energy. The different kinematic of these events leads to two kind of π^0 in the selected events,

- photons are identified and paired to reconstruct π^0 masses.
- high energy π^0's often lead to single clusters in the electromagnetic calorimeter. In these cases the energy distribution of the showers allows to identify if the clusters are coming from a π^0 decay.

The first step of π^0 reconstruction consists on looking for photon clusters in the electromagnetic calorimeter. The method to identify photons is described in 4.3.1, where a likelihood technique is used to separate real photons from the "fake" photons produced in hadronic and electromagnetic showers or due to the overlapping of different showers. The second step consists on pairing all photon candidates and defining a π^0 global estimator, which is described in 4.3.2. An explicit description of the method can be found in [26].

4.3.1 Photon Identification.

The photons are identified following two different techniques.

Converted photons

To identify photons which convert inside the tracking volume all the tracks in one hemisphere with opposite charge are paired, and one of them is required to be an electron, see section 4.2. The candidates are required to have an invariant mass smaller than 30 MeV/c^2 and the minimal distance between the two helices in the plane normal to the beam direction must be smaller than 0.5 cm. The radial distribution of the materialization point for converted photons is shown in 4.1, where the good agreement between data and the Monte Carlo simulation of the ALEPH detector shows that the amount of material in the detector is properly modeled.

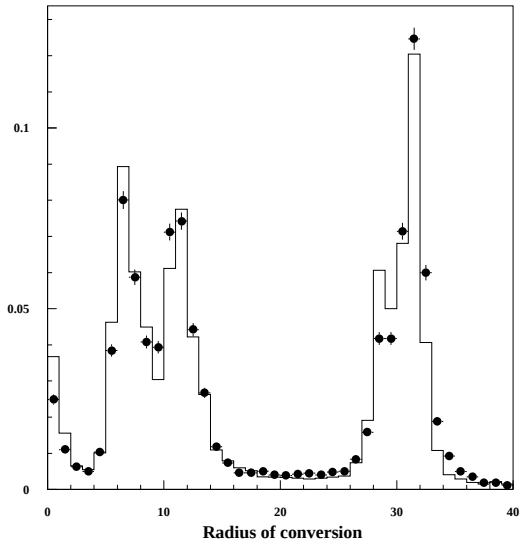

Figure 4.1: Radial distance to the beam axis for the converted photons for the simulation (solid histogram) and data (points with error bars

.

ECAL photons

The clustering algorithm for the photon reconstruction is described in [18]. The first ECAL stack is scanned in order of decreasing energy. An storey without a more energetic neighbour defines a new cluster. The rest of the storeys are assigned to the cluster of their highest energy neighbour. Two storeys are considered as neighbours

only if they share one of the faces. The same procedure is applied to the second and third stacks, and now the algorithm looks first for a neighbour in the previous stack. The cluster is retained like a photon if its energy is above 350 MeV and the distance to the closest charged track is larger than 2 cm.

The energy of the four central towers is used to estimate the energy of the photon cluster. The direction of the photon is obtained from the barycenter of energy deposition corrected by the finite size of the calorimeter cells.

In order to distinguish fake photons from photons originating from π^0 decays (or other physical sources), several estimators are constructed and a likelihood method is used. For every photon the following estimator is defined:

$$P_\gamma = \frac{P^{genuine}}{P^{genuine} + P^{fake}} \tag{4.2}$$

where P^i is the photon estimator of type i, which is given by

$$P^i = \prod_j \P_j^i(z_j) \tag{4.3}$$

and $\P_j^i(z_j)$ is the probability density for the hypothesis of type i associated to the variable z_j.

The following discriminating variables, z_j, are used to distinguish between genuine and fake photons:

- the energy fraction in the first and second ECAL stack,
- the energy fraction outside the four central towers defining an ECAL cluster,
- the transverse size of the photon shower,
- the distance to the nearest photon,
- and the distance between the photon barycenter and the closest charged track.

Reference distributions are obtained from Monte Carlo simulations for genuine and fake photons.

4.3.2 π^0 reconstruction

π^0 with two resolved γ's

The first step of π^0 reconstruction consists on pairing all the identified photons of one hemisphere, considering all the possible combinations. A π^0 estimator, $D^{\pi^0}_{i,j}$, is constructed for all the photons inside a cone of 45° around the thrust axis. The estimator is defined as

$$D^{\pi^0}_{i,j} = P_{\gamma_i} P_{\gamma_j} P_{\pi^0}, \tag{4.4}$$

where P_{π^0} is the probability coming from a π^0-mass constrained fit, and the P_{γ_i} are the photon estimators described in subsection 4.3.1.

A dependence of the invariant mass with the π^0 energy is shown in fig. 4.2. This dependence is a consequence of the overlapping of the two photons in the calorimeter. The dependence show at fig. 4.2 has a different behaviour for data and Monte Carlo. This effective π^0 mass dependence is taken into account to obtain the P_{π^0}. The effective π^0 dependence is taken separately for data and Monte Carlo.

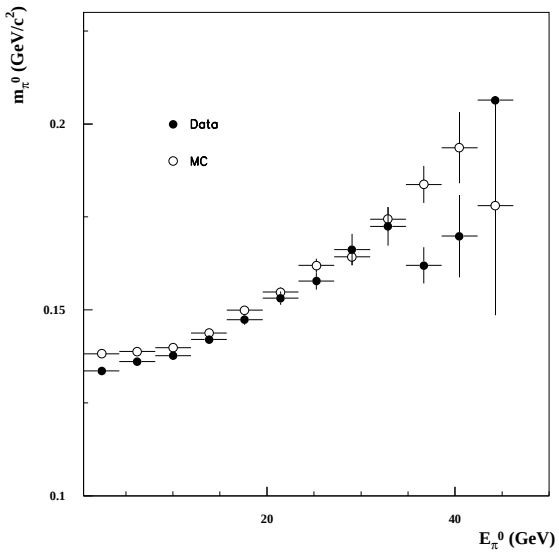

Figure 4.2: Dependence of the π^0 invariant mass with the energy for data and Monte Carlo.

Once the π^0 is identified a second kinematically constrained fit is done to the nominal π^0 mass. This fit improves the π^0 energy resolution as it is shown in [26].

π^0 with unresolved γ's

As the π^0 energy increases it becomes more difficult to resolve the two photons and the clustering algorithm eventually gives a single cluster. An energy-weighted moment analysis can be done for the two-dimensional energy distribution in the plane normal to the shower direction. The second moment provides a measure of the $\gamma\gamma$ invariant mass. All the photons not entering the selection for resolved π^0's but having an invariant mass larger than 100 MeV/c^2, are kept as π^0 candidates. Clusters with invariant mass smaller than 100 MeV/c^2 correspond mainly to radiative photons or π^0 with a lost photon. The invariant mass for π^0 with unresolved γ's is shown in Fig.4.3 for data and Monte Carlo.

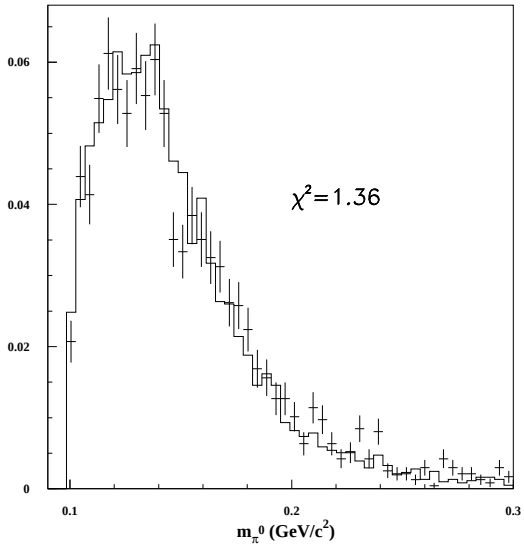

Figure 4.3: Unresolved π^0 invariant mass for data and Monte Carlo (solid line histogram).

4.4 Event selection

The final $\tau^+\tau^-$ selection is based on the identification of the $\tau^\pm$ decay channel. Every event is divided into to hemispheres along the thrust axis computed with the charged tracks and neutral clusters in the calorimeters. The leading track at each hemisphere is identified following the technique described in 4.2. The technique

described in 4.3 to identify π^0 is applied to all the hemispheres with the leading track identified as a $\pi^{\pm}$.

A ρ particle is identified when the invariant mass, m_ρ, of an identified π^0-$\pi^{\pm}$ pair falls inside the interval (0.44, 1.1) GeV/c^2. The invariant mass distribution for data and Monte Carlo is shown in fig.4.4. Both distributions agree all over the interval of masses considered.

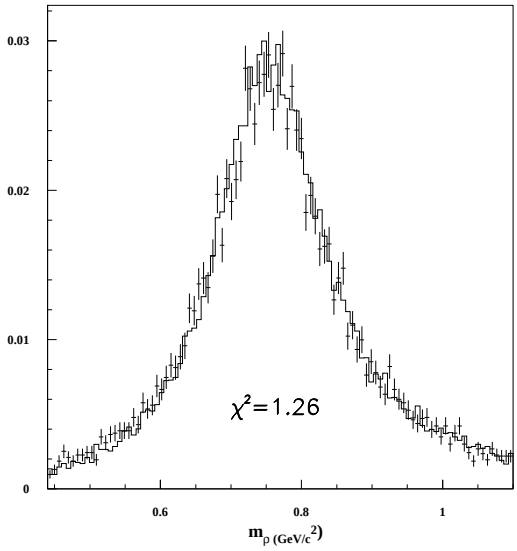

Figure 4.4: $\rho^{\pm}$ invariant mass for data and Monte Carlo (solid line histogram).

An event is selected when both hemispheres have been identified to be $e^{\pm}$, $\mu^{\pm}$, $\pi^{\pm}$, $\rho^{\pm}$. In addition, it is required that no identified objects, other than those mentioned, be present in any of the hemispheres, except those neutral clusters identified to be "fake" photons.

The background is coming from $e^+e^- \to e^+e^-$ (Bhabha events) and $e^+e^- \to \mu^+\mu^-$ events and $\tau^+\tau^-$ events with misidentified decay channels, although some contribution from $q\bar{q}$ and cosmic rays is still present in the selected sample. This background is reduced by means of additional cuts.

The Bhabhas and dimuon contaminations are reduced rejecting the e^+e^- and $\mu^+\mu^-$ events. The sensitivity of the l^-l^+ ($l = e, \mu$) decay channels is in any case small, at the level of 4%. Finally, six classes of events are considered: $e^{\pm}\mu^{\mp}$, $l^{\pm}\pi^{\mp}$, $l^{\pm}\rho^{\mp}$, $\pi^{\pm}\pi^{\mp}$, $\pi^{\pm}\rho^{\mp}$ and $\rho^{\pm}\rho^{\mp}$. It is not necessary to distinguish between electrons

and muons because both decays have the same dependence of the cross-section with the acollinearity and aplanarity angles, as explained in Appendix A.

The $\pi-(\mu/e)$ misidentification leads to a significative background from Bhabha and dimuon events in the $l^{\pm}\pi^{\mp}$ channel. This background is reduced rejecting the events with a total event energy larger than 80 GeV. Fig. 4.5 shows the total energy distribution where the contamination from e^+e^- and $\mu^+\mu^-$ events is clearly visible.

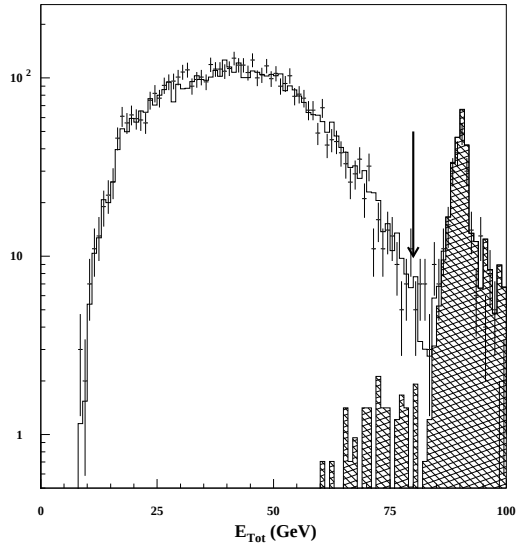

Figure 4.5: Total energy of $\pi^{\pm}l^{\mp}$ events for data and Monte Carlo (solid line histogram). The hatched histogram shows the e^+e^- and $\mu^+\mu^-$ background contribution. The arrow marks the cut applied to reduce the background.

The main $\tau^+\tau^-$ background is due to the $\rho-\pi$ and $(\rho/\pi)-n\pi's$ misidentification. Only the events with $|\cos\theta_1|$ <0.85 are selected, where θ_1 is the polar angle of the negative τ decay particle. This cut reduces the possibility of loosing particles within the beam pipe. The sensitivity to the transverse spin correlations goes as $\sin^2\theta_1$ and therefore the rejected events give a very small contribution to the final statistical error. On the other hand, this angular cut barely coincides with the acceptance of the inner wafer of the VDET detector, so the selected events are included in the acceptance of all the tracking devices.

The analysis is done within the acolinearity range $0.5^\circ < (180^0 - \epsilon) < 9.0^\circ$ for all the channels, except for the $\rho^+\rho^-$ in which the upper acollinearity limit is fixed

to 4.0°. These cuts reduce the $\gamma\gamma$, the Bhabha, and the dimuon contaminations, while the loss of statistics and sensitivity is negligible.

The cosmic-ray contamination has been reduced after the rejection of the $\mu^+\mu^-$ events, but, an additional cut is applied on the track impact parameters. One the tracks in the event should verify the conditions: $|d_0| < 1$ cm and $|z_0| < 5$ cm, which selects particles produced at the interaction point.

An additional cut is applied to increase the sensitivity to the transverse spin correlations. The momentum of identified particle should be greater than 4.0 GeV/c. This cut removes a momentum interval where the function $Q_3^{ij}(\epsilon)$ turns out to have the opposite sign that the average for particles with momentum greater than 4.0 GeV/c, and therefore it increases the averaged sensitivity as a function of the acollinearity.

Figure 4.6 shows the distribution of the invariant mass for data and $\tau^+\tau^-$ Monte Carlo (the $q\bar{q}$ Monte Carlo is not included). As it can be seen, this distribution is well explained by the Monte Carlo, which implies that the possible remaining $q\bar{q}$ background is negligible.

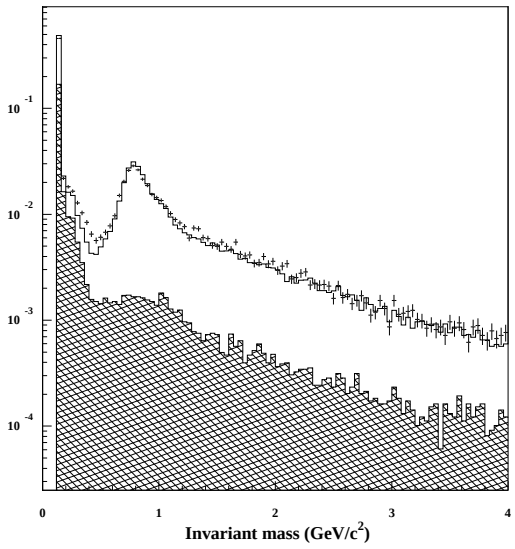

Figure 4.6: Invariant mass distribution. The points are the data, the solid histogram the $\tau^+\tau^-$ Monte Carlo prediction and the hatched histogram the Monte Carlo prediction for misidentified data. The discrepancies below the ρ peak are due to the defect of "fake photons" in the Monte Carlo simulation.

The purity of the π and ρ identification is increased by requiring the total energy in one hemisphere to be assigned to identified particles. The hemispheres containing π's should verify $E_i - E_i^{iden} < 12.0$ GeV, where E_i^{iden} is the energy of the identified particle and E_i is the neutral plus charged energy of the i^{th} hemisphere. These cuts remove the events where the neutral energy has not been properly assigned to an identified particle. Figures 4.7 and 4.8 show the variable $E_i - E_i^{iden}$ for the π and ρ hemispheres predicted by the Monte Carlo where the good and the bad channel identifications are separated.

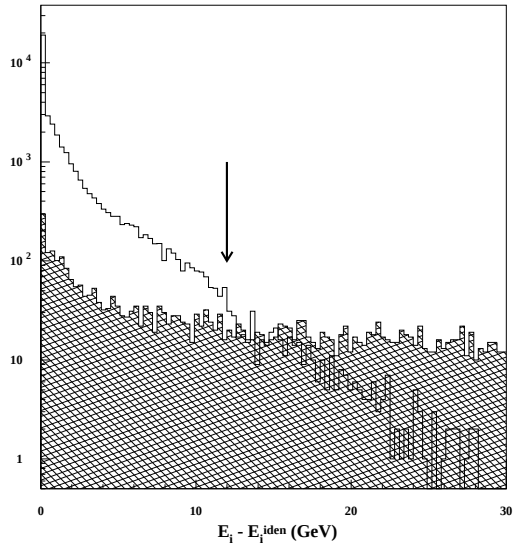

Figure 4.7: $E_i - E_i^{iden}$ for the $\pi^{\pm}$ hemispheres. The solid and the hatched histograms correspond to the events with a good identification and to the misidentified events respectively. The arrow shows the position where the cut is applied.

4.5 Event selection efficiency and purity

The final selection efficiencies are computed with the Monte Carlo. The results are presented in Table 4.1 where only the statistical errors are considered.

The channel mixing due to decay mode misidentification is calculated with a full detector Monte Carlo simulation. Each generated τ decay is considered in this calculation. The mixing matrix is defined such that the $i-j$ element, M_i^j, is defined as the fraction of events classified as belonging to the "i" channel which is generated

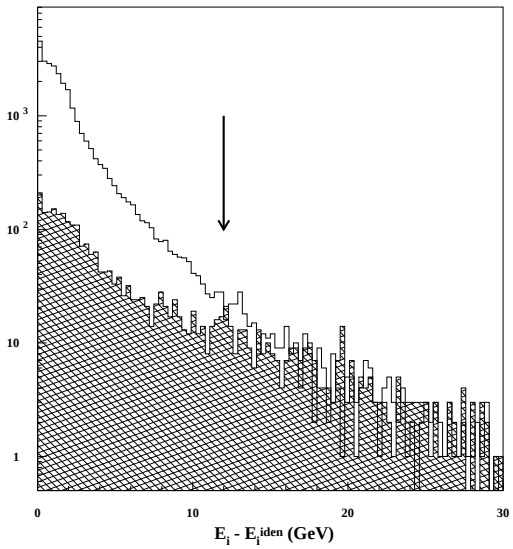

Figure 4.8: $E_i - E_i^{iden}$ for the $\rho^{\pm}$ hemispheres. The solid and the hatched histograms correspond to the events with a good identification and to the misidentified events respectively. The arrow shows the position where the cut is applied.

in the "j" channel. To include any possible bias from the cuts and detector effects the matrix is computed after the $\tau^+\tau^-$ event selection described above. The matrix is shown in Table 4.2, where only the statistical errors are included.

Channel	Efficiency (%)
$e^{\pm}\mu^{\mp}$	39.90 ± 0.56
$l^{\pm}\pi^{\mp}$	44.26 ± 0.52
$l^{\pm}\rho^{\mp}$	31.94 ± 0.30
$\pi^{\pm}\pi^{\mp}$	48.16 ± 1.4
$\pi^{\pm}\rho^{\mp}$	35.24 ± 0.55
$\rho^{\pm}\rho^{\mp}$	22.69 ± 0.41

Table 4.1: Selection efficiency for the different decay channels, the errors are due to the MC statistics.

Clase	e/μ	π	ρ	$\pi\pi^0\pi^0$	$n\pi/K$
e/μ	0.9947 ± 0.0004	0.0039 ± 0.0003	0.0011 ± 0.0002	0.0001 ± 0.0001	0.0001 ± 0.0001
π	0.0152 ± 0.0009	0.9061 ± 0.0020	0.0573 ± 0.0019	0.0191 ± 0.0010	0.0022 ± 0.0003
ρ	0.0003 ± 0.0001	0.0027 ± 0.0003	0.9302 ± 0.0015	0.0591 ± 0.0013	0.0078 ± 0.0005

Table 4.2: Fraction of the generated i clase events identified in j clase, M_i^j. The generated classes are given in the first row, and the reconstructed clases in the first column.

Chapter 5

Measurement of the transverse spin correlations

The method to get the transverse spin correlations is to compare the sample of selected data with the prediction of the theory leaving free the A_{TT} and A_{TN} parameters to model the spin correlations. An event by event likelihood method is selected to fit both transverse spin parameters, since it is this method that maximizes the sensitivity of the data. The transverse spin components are weighted by the kinematical factor $\frac{2m_\tau}{M_Z} \approx 0.04$ with respect to the longitudinal spin components, see 2.20, so a method providing the maximum sensitivity is needed to get a reasonable statistical error.

5.1 The likelihood method

An event by event likelihood fit is used to get he maximum sensitivity from the sample of selected data. The following expression is minimized:

$$\mathcal{L} = \sum_{i,j} \sum_{n=1}^{N_{events}^{ij}} \ln \left(\sum_{kl} M_i^k M_j^l \frac{d^3\Gamma_{kl}}{d\epsilon \; d\cos\theta_1 \; d\phi}(\epsilon, \phi, \theta_1; A_{TT}, A_{ATN}) \right) \qquad (5.1)$$

where,

- i and j are the identified τ decay classes ($e^\pm$, $\mu^\pm$, $\pi^\pm$ or $\rho^\pm$),

- k and l are the channels contributing to i and j due to the mixing described by the matrices M_i^k and M_j^l as explained in section 4.5,
- $d^3\Gamma_{kl}(\epsilon, \phi, \theta_1; A_{TT}, A_{ATN})/d\epsilon\ d\cos\theta_1\ d\phi$ is the cross section of the $e^+e^- \to \tau^+\tau^- \to d_k^+ d_l^- ...$ reaction computed in eq. 2.59 and 2.60, and modified to include the experimental effects from the selection and the effect of the Initial State Radiation, see section 5.1.1,
- N_{events}^{ij} is the number of selected events of class ij.

5.1.1 The Initial State Radiation

The initial state radiation, ISR, causes that the beam and the two particles in the final state tend to collapse in the same plane. This fact implies that the aplanarity angle ϕ tends to 0 ° or ± 180 °. It has been shown [5] that the contribution from the ISR is mainly due to the boost of the center of mass in the direction of the initial beam. The ISR is corrected by redefining the cross section as follows:

$$\frac{d^3\Gamma_{kl}}{d\epsilon\ d\cos\theta_1\ d\phi} = \int_0^{0.2} dx H(x) \frac{d^3\sigma_{kl}(M_Z^2(1-x))}{d\epsilon''\ d\theta'\ d\phi'} \frac{\partial(\epsilon', \theta', \phi')}{\partial(\epsilon, \theta_1, \phi)} \frac{\partial\epsilon''}{\partial\epsilon'} \tag{5.2}$$

where the next to leading order Initial State Radiation function, $H(x)$, is given by [27]

$$H(x) = \beta x^{\beta-1}(1 + \frac{3}{4}\beta + \frac{\alpha}{\pi}(\frac{\pi^2}{3} - \frac{1}{2})) - \frac{\beta}{2}(2 - x), \tag{5.3}$$

where β is defined as

$$\beta = \frac{2\alpha}{\pi}(\ln\frac{s}{m_e^2} - 1), \tag{5.4}$$

and x is the fraction of the beam energy carried by the initial state photon.

The jacobian, $\partial(\epsilon'', \theta', \phi')/\partial(\epsilon, \theta_1, \phi)$, accounts for the change in the three angles ϵ, θ_1, and ϕ due to the boost. The $Z^0-\gamma$ interference terms in the angular distribution $d\sigma_{kl}(M_Z^2(1-x))/d\epsilon'\ d\cos\theta'\ d\phi'$ are fixed to the Standard Model predictions, see Table 2.3.

In order to use the same $Q_i(\epsilon)$ that are computed at the Z^0 center of mass energy the value of the acollinearity angle used in the angular distribution should be recomputed accordingly. As shown in [7], the $Q_i(\epsilon)$ are effectively functions of $\gamma(180^\circ - \epsilon) = \sqrt{s}/2m_\tau(180^\circ - \epsilon)$, and therefore the equivalent acollinearity for the Initial State Radiation events is:

$$(180^\circ - \epsilon'') \quad = \quad (180^\circ - \epsilon')\sqrt{1-x} \tag{5.5}$$

The use of ϵ'' instead of ϵ' is equivalent to compute the $Q_i(\epsilon)$ functions for each center of mass energy. This approximation is valid for $\gamma^{-1} \ll 1$, where γ^{-1} is smaller than 5 % for values of the radiation parameter, x, smaller than 0.2, which is the limit value used in the integration.

An alternative description of the initial state radiation function $H(x)$ has been obtained using the KORALZ [28] Monte Carlo. All the photons radiated along the beam pipe, $|\cos(\theta_{rad})| > 0.95$, are considered, and the obtained x distribution is corrected by the $e^+e^- \to \tau^+\tau^-$ cross-section to compute the radiation function $H(x)$. The comparison between the two radiation functions, the analytical and the one computed from KORALZ Monte Carlo, could be included, if needed, as a systematic uncertainties due to the modelization of the initial state radiation function.

5.1.2 nπ background

The contamination from the channel $\tau \to n(\pi)\nu$ is due to the loss of one of the pions. The missing particle cancels the sensitivity to the transverse spin correlation. This fact has been checked generating, with the TAUOLA Monte Carlo, a sample of nπ τ decays and removing randomly one of the pions. The computed value for the $Q_3^{ij}(\epsilon)$ function is always compatible with zero, and therefore suppresses the sensitivity to the transverse spin correlations. This effect is taken into account in the fit. The cross section $d^3\Gamma_{kl}/d\epsilon\, d\cos\theta_1\, d\phi$ does not include the term in $Q_3(\epsilon)$ when the migration happened from one channel of larger multiplicity to a channel with less multiplicity.

5.1.3 The $\tau^{\pm} \to K^{\pm}\nu_{\tau}$ decay channel

In order to increase the $\tau^+\tau^-$ selection efficiency we will not distinguish between the $\pi^{\pm}$ and the $K^{\pm}$ decay products. Therefore the $Q_n^{ij}(\epsilon)$ functions are redefined as

$$\begin{aligned} Q_n^{i\pi}(\epsilon) &\to W_\pi Q_n^{i\pi}(\epsilon) + W_K Q_n^{iK}(\epsilon),\ i \neq \pi \\ Q_n^{\pi\pi}(\epsilon) &\to W_\pi W_\pi Q_n^{\pi\pi}(\epsilon) + W_K W_K Q_n^{KK}(\epsilon) + 2W_\pi W_K Q_n^{\pi K}(\epsilon), \end{aligned} \tag{5.6}$$

with $n = 1, 2, 3$, $W_\pi = B_{\tau\to\pi\nu}/[B_{\tau\to\pi\nu} + B_{\tau\to K\nu}]$, and $W_K = 1 - W_\pi$, where the B's are the branching ratios from the PDG tables [16].

5.1.4 Correction of the ρ asymmetries

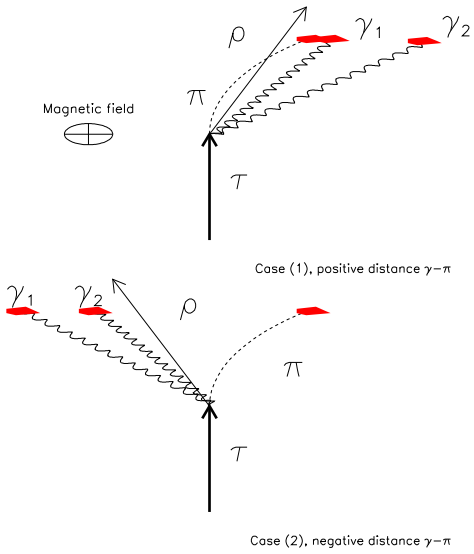

Figure 5.1: ϕ symmetry breaking in the ρ reconstruction due to the magnetic field. In the first case the distance $D_{\pi-\gamma}$ is positive and in the second case $D_{\pi-\gamma}$ is negative where the reconstruction is more efficient.

The decay of the ρ meson into $\pi\pi^0$ produces an angular asymmetry in the the ρ identification due to the overlapping of the $\pi^{\pm}$ hadronic shower and the γ's electromagnetic shower. The magnetic field bends the charged pion breaking the

Class	$A_{\rm TT}^{bias}$	$A_{\rm TN}^{bias}$
l^+l^-	-0.12 $\pm$ 0.46	0.09 $\pm$ 0.46
$l^\pm\pi^\mp$	0.10 $\pm$ 0.15	0.12 $\pm$ 0.15
$l^\pm\rho^\mp$	-0.40 $\pm$ 0.27	-0.26 $\pm$ 0.27
$\pi^+\pi^-$	0.02 $\pm$ 0.14	-0.12 $\pm$ 0.14
$\pi^\pm\rho^\mp$	0.03 $\pm$ 0.18	-0.40 $\pm$ 0.18
$\rho^\pm\rho^\mp$	0.48 $\pm$ 0.39	0.08 $\pm$ 0.41

Table 5.1: Values of the transverse spin correlation from the fit to the Monte Carlo.

azimuthal symmetry of its production with respect to the π^0, see Fig.5.1. This effect is corrected by Monte Carlo as follows.

The Koralz Monte Carlo, which is the standard Monte Carlo used in LEP to describe the $\tau^+\tau^-$ final state, does not include transverse spin correlations. A fit to Monte Carlo generated events should thus give a zero value for the $A_{\rm TT}$ and $A_{\rm TN}$ correlation parameters. If a fit is performed, the results are indeed zero for all channels except those including ρ's, as shown in Table 5.1. It is in effect the ρ asymmetry mentioned above that induces these non-zero values. This asymmetry in the ρ's is well described in the Monte Carlo as shown in figure 5.2. The values obtained from the fit to the Monte Carlo channels is taken as a bias on $A_{\rm TT}$ and $A_{\rm TN}$ due to this effect. These values are subtracted from those obtained when fitting the real data, and the statistical errors in the Monte Carlo fit are propagated accordingly, and included as a systematic as explained later.

This procedure can be justified analytically. For simplicity the $\cos(2\phi)$ is considered in what follows. The used Monte Carlo has no transverse spin correlation effects, that means that the cross section can be described as, $\sigma_0(\epsilon, \theta_1)$. The detector distortion is just an efficiency dependence, $f(\phi)$, with the aplanarity angle, ϕ.

The cross section turns out to be,

$$f(\phi)\sigma_0(\epsilon,\theta_1) \tag{5.7}$$

Fitting the Monte Carlo to the predicted cross-section, the dependence is parametrized as,

$$f(\phi)\sigma_0(\epsilon,\theta_1) \;\;\rightarrow\;\; \sigma_0(\epsilon,\theta_1) + A_{\rm TT}^{bias}\,\sigma_1(\epsilon,\theta_1)cos(2\phi), \tag{5.8}$$

This parametrization describes the effect since the only term in $f(\phi)$ that affects the result is $cos(2\phi)$. The other terms are orthonormal and have no contribution to the transverse spin correlation.

The total cross-section corrected by the aplanarity efficiency turns out to be,

$$\begin{aligned} f(\phi)(\sigma_0(\epsilon,\theta_1) + A_{\rm TT}\sigma_1(\epsilon,\theta_1)\cos(2\phi)) \;\; &= \;\; \sigma_0(\epsilon,\theta_1)) + A_{\rm TT}^{bias}\sigma_1(\epsilon,\theta_1)\cos(2\phi) \\ &\quad + A_{\rm TT}\sigma_1(\epsilon,\theta_1)\cos(2\phi) \\ &\quad + \vartheta(\sigma_1(\epsilon,\theta_1)). \end{aligned} \tag{5.9}$$

The additional terms, $\vartheta(\sigma_1(\epsilon,\theta_1))$, have a dependence with the aplanarity angle which do not affect the $A_{\rm TT}$ and $A_{\rm TN}$ correlations since they are orthonormal to $\cos(2\phi)$ and $\sin(2\phi)$. There is also a small contribution independent of ϕ that we can neglect since $\sigma_1 << \sigma_0$. The measured value in the data fits, using this parametrization, turns out to be,

$$\begin{aligned} A_{\rm TT}^{meas} &= A_{\rm TT} + A_{\rm TT}^{bias} \text{ and,} \\ A_{\rm TN}^{meas} &= A_{\rm TN} + A_{\rm TN}^{bias} \end{aligned}$$

5.1.5 Correction of the $Q_i(\epsilon)$ functions

The $Q_n(\epsilon)$, $n = 1, 2, 3$, functions have a different intrinsic dependence of the efficiency reconstruction with the momentum of the two identified tracks. These differences should be taken into account for the computation of the $Q_n(\epsilon)$ functions. Those $Q_n(\epsilon)$ functions are computed by weighting the TAUOLA Monte Carlo events, see Appendix A, with the momentum dependence of the channel reconstruction efficiency obtained from the full detector simulation. The efficiency

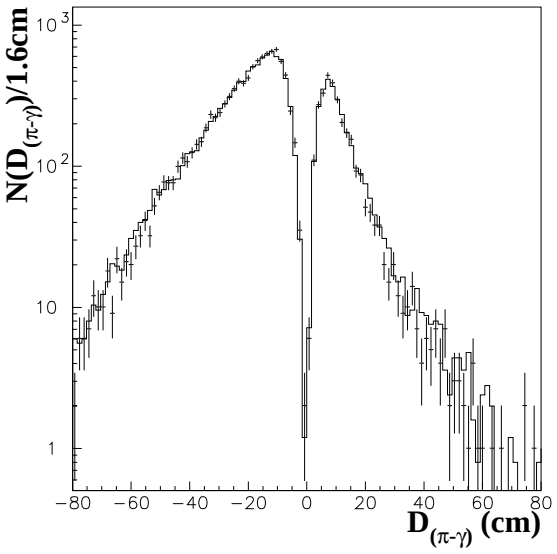

Figure 5.2: Minimum distance from a γ of a π^0 decay and the $\pi^{\pm}$ track extrapolation from a ρ decay into ECAL. The data (points with error bars) and the MC prediction (solid histogram) agree in the whole spectrum.

reconstruction, after the detector and the cut effects, versus the momentum of the identified particle are shown in Figs. 5.3, 5.4, 5.5, 5.6 and 5.7. The ρ channel is considered separately when the ρ is well identified. If the ρ is not well identified the momentum dependence is not the same as it is shown in Figs. 5.5 and 5.6.

The Monte Carlo predictions for the momentum distributions are checked in Figs. 5.8, 5.9 and 5.10. The agreement is good in each case.

5.2 Results of the fit

The values of the transverse spin correlations obtained from the likelihood fit, based on 80 pb^{-1} of the data collected by ALEPH in 1992, 1993 and 1994 on the peak of the Z^0 resonance, are:

$$\begin{aligned} A_{TT} &= 1.06 \pm 0.13 \\ A_{TN} &= 0.08 \pm 0.13 \end{aligned}$$

where only the statistical error of the fit is presented. The correlation between the two values turns out to be close to zero. The two dimensional χ^2 curves are shown

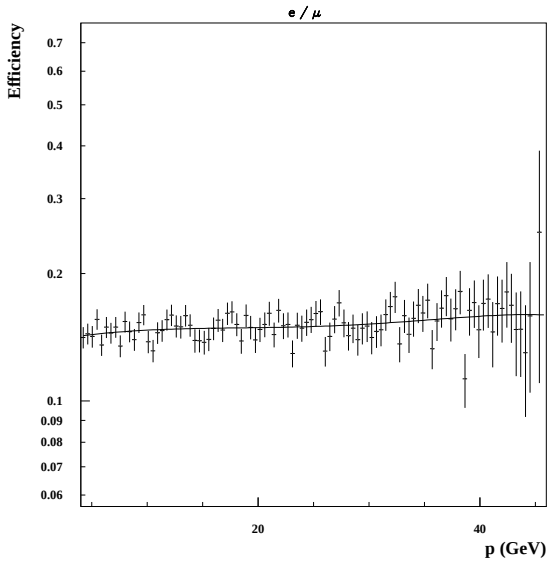

Figure 5.3: Reconstruction efficiency as a function of the momentum for the e/μ hemispheres.

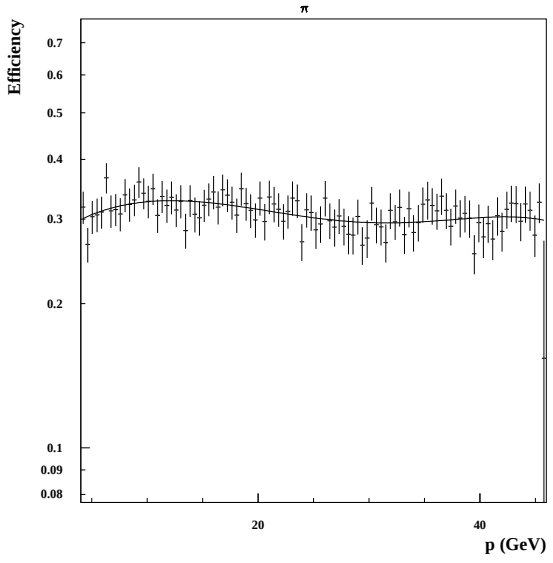

Figure 5.4: Reconstruction efficiency as a function of the momentum for the π hemispheres.

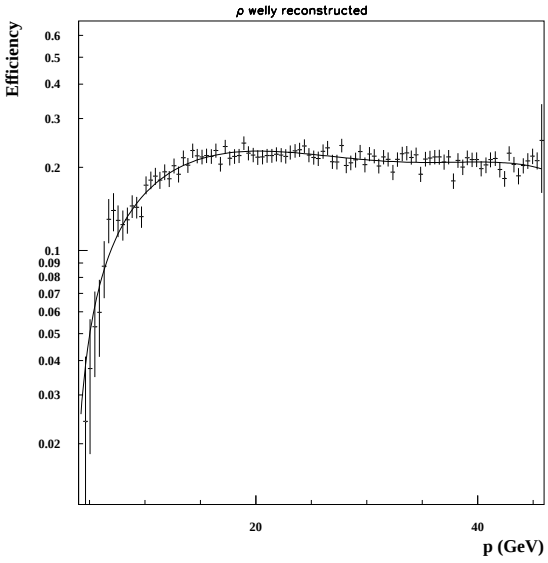

Figure 5.5: Reconstruction efficiency as a function of the momentum for the correctly reconstructed ρ hemispheres.

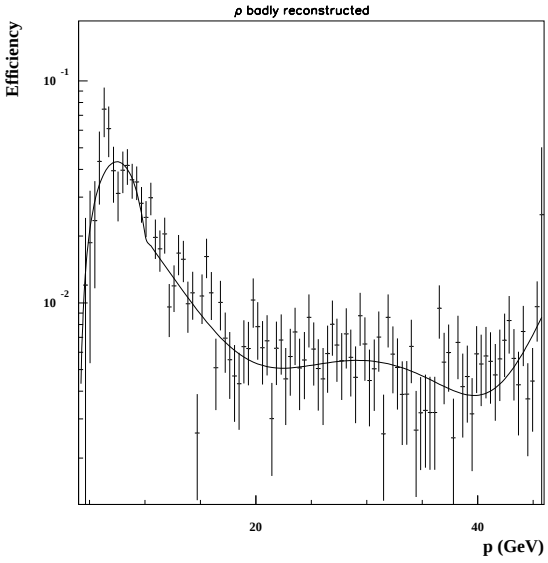

Figure 5.6: Reconstruction efficiency as a function of the momentum for the ρ particles when they are misidentified.

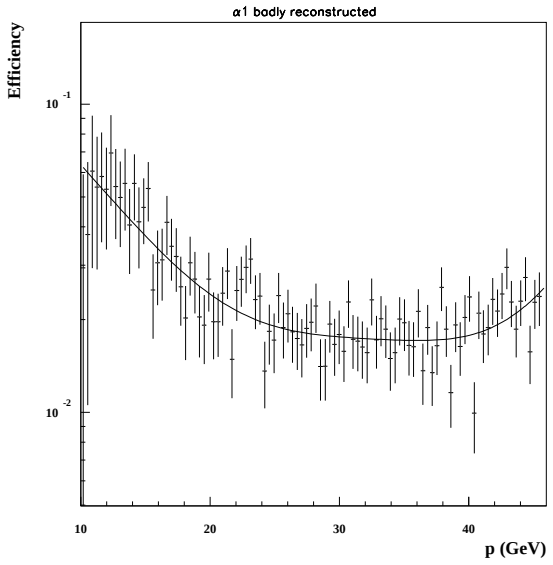

Figure 5.7: Reconstruction efficiency as a function of the momentum for the a_1 hemispheres when they are misidentified .

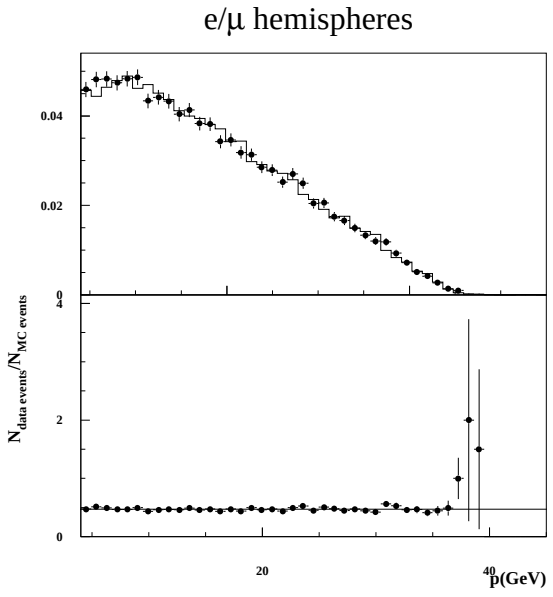

Figure 5.8: Comparison between the selected e/μ momentum distribution for data and MC. The lower plot shows the ratio between both distributions. The agreement is good.

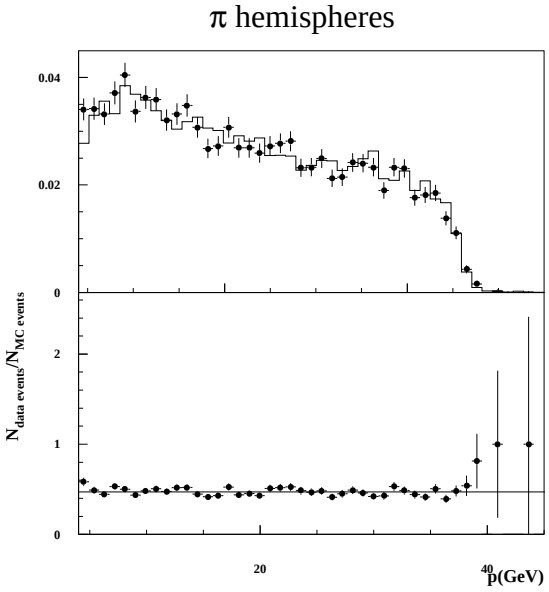

Figure 5.9: Comparison between the selected π momentum distribution for data and MC. The lower plot shows the ratio between both distributions. The agreement is good.

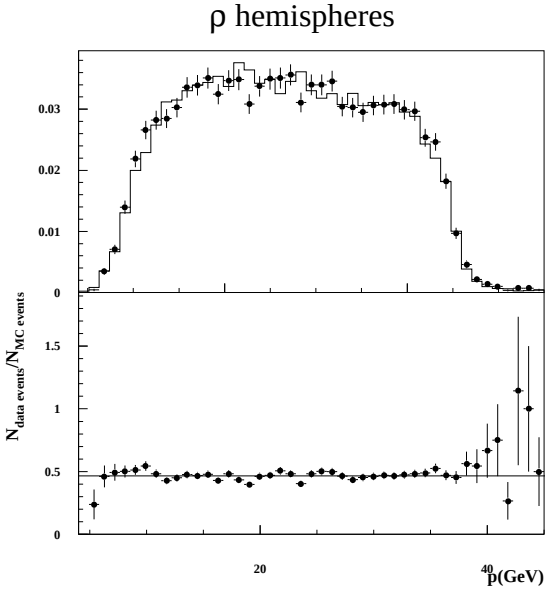

Figure 5.10: Comparison between the selected ρ momentum distribution for data and MC. The lower plot shows the ratio between both distributions. The agreement is good.

at Fig.5.11. The A_{TT} and A_{TN} values for data of each year are shown in Table 5.2. The A_{TT} and A_{TN} spin correlations in these periods are mutually consistent among themselves and with the Standard Model predictions, $A_{TT} = 0.989 \pm 0.001$ for $\sin^2\theta_{\rm W} = 0.2315 \pm 0.0008$[16] and $A_{TN} = 0$.

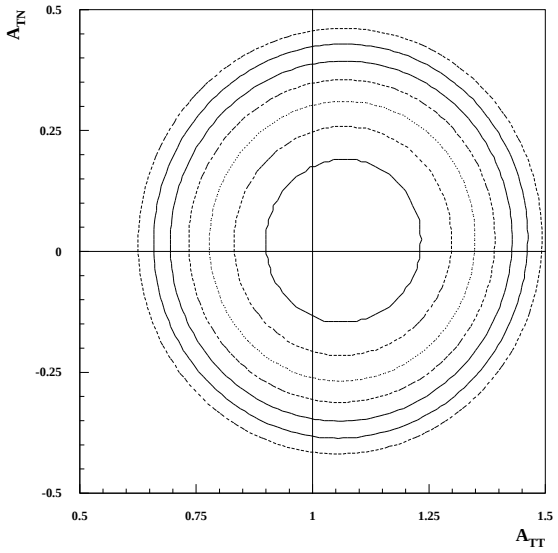

Figure 5.11: Correlation between the A_{TT} and A_{TN}. The lines show the levels from 1 up to 7 σ. The straight lines show the Standard Model Prediction.

The "universality" of the transverse spin correlations has been checked computing A_{TT} and A_{TN} channel by channel independently. The results are shown in Table 5.3. The small contribution from the channels involving the ρ and the pure leptonic τ decays are explained by the small sensitivity of these channels, see Appendix B.

5.3 Systematic checks

The cross section for the $\tau^+\tau^-$ production and decay shown in formulae 2.59 and 2.60 is a function of three angles: the acollinearity (ϵ), the polar (θ_1) and the aplanarity (ϕ). The functional dependence on these angles of the cross section at the Z^0 center of mass energy can be explicitly written as:

Year	A_{TT}	A_{TN}
1992	1.25 $\pm$ 0.22	0.08 $\pm$ 0.24
1993	0.94 $\pm$ 0.28	-0.11 $\pm$ 0.27
1994	1.04 $\pm$ 0.17	0.20 $\pm$ 0.17
Total	1.06 $\pm$ 0.13	0.08 $\pm$ 0.13
	$\chi^2 = 0.9 \;\; C.L. = 63.8\%$	$\chi^2 = 0.9 \;\; C.L. = 63.8\%$

Table 5.2: Transverse spin correlation as a function of the running period. Only the statistical error is shown.

$$\frac{d^3\sigma(\epsilon,\theta_1,\phi)}{d\epsilon d\cos\theta_1 d\phi} = F(\epsilon,\theta_1)(1. + Sen(\epsilon,\theta_1)(A_{TT}\cos(2\phi) + A_{TN}\sin(2\phi)) \quad (5.10)$$

The values of the transverse spin correlations come from the asymmetry in the $\cos(2\phi)$ and $\sin(2\phi)$, but weighted by the factor $Sen(\epsilon,\theta)$ which accounts for the sensitivity of each event to this asymmetry. The incorrect modeling of the sensitivity by the theory would provoke a dependence of the measured transverse spin correlation with the acollinearity and polar angles. This can be checked by binning the acollinearity and the polar angles and computing the transverse spin correlations within each of the resulting intervals. No dependence has been found, as it is shown in Figs. 5.12 and 5.13, for the acollinearity and the polar angles respectively.

The total cross section ($F_0^{ij}(\epsilon)$) as a function of the acollinearity angle, ϵ, is compared with the theoretical cross section used for the likelihood fit in Figs. 5.14 to 5.19. The theoretical functions are normalized to the number of events. The hatched histogram shows the predicted τ background events. There is an agreement between the data and the theoretical cross section once the latter has been corrected by the momentum reconstruction efficiency.

Decay mode	A_{TT}	A_{TN}	Contribution to the total error
$e^{\pm}\mu^{\mp}$	0.92 $\pm$ 0.70	-0.92 $\pm$ 0.71	3.2%
$l^{\pm}\pi^{\mp}$	0.79 $\pm$ 0.24	-0.01 $\pm$ 0.24	27.1%
$l^{\pm}\rho^{\mp}$	1.25 $\pm$ 0.50	0.12 $\pm$ 0.51	4.6%
$\pi^{+}\pi^{-}$	1.03 $\pm$ 0.19	0.07 $\pm$ 0.20	41.7%
$\pi^{\pm}\rho^{\mp}$	1.36 $\pm$ 0.32	0.38 $\pm$ 0.32	20.8%
$\rho^{+}\rho^{-}$	2.08 $\pm$ 0.71	0.68 $\pm$ 0.75	2.65%
Total	1.06 $\pm$ 0.13	0.08 $\pm$ 0.13	
	$\chi^2 = 4.4$ $C.L. = 49.3\%$	$\chi^2 = 3.6$ $C.L. = 65.4\%$	

Table 5.3: Transverse spin correlation for every decay mode. The last column shows the contribution of every channel to the averaged value. Only the statistical error is shown.

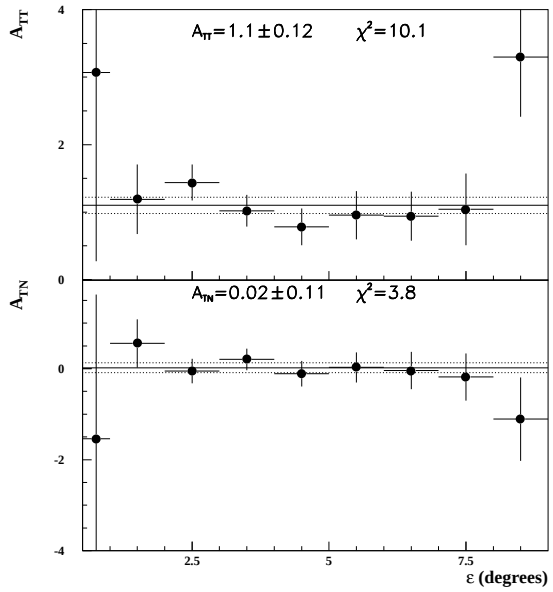

Figure 5.12: The A_{TT} and A_{TN} observable for different acollinearity angle intervals.

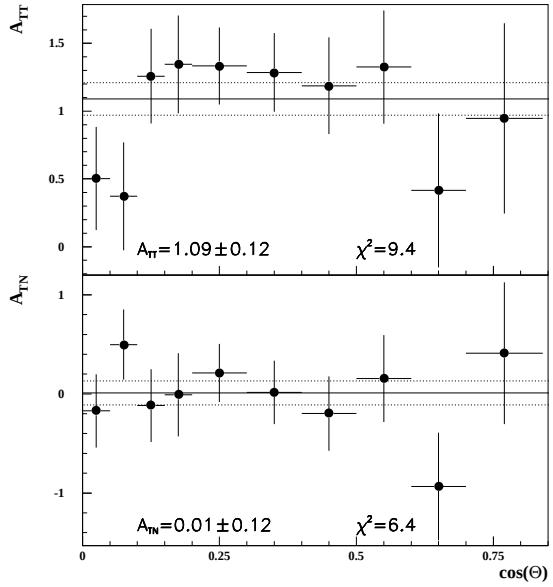

Figure 5.13: The A_{TT} and A_{TN} observable for different polar angle intervals.

The aplanarity dependence of the different channels is compared with the predictions of the SM ($A_{TT} = 0.989$ and $A_{TN} = 0.0$) in Figs. 5.20 to 5.25. The predicted $\cos(2\phi)$ dependence is clearly visible for each of the analysed channels.

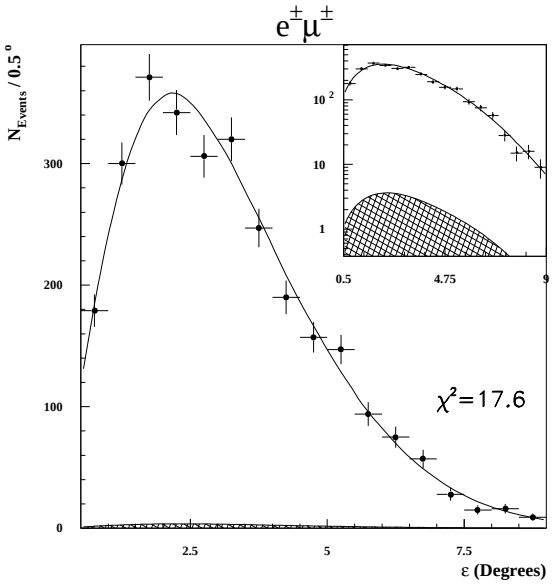

Figure 5.14: Comparison of the predicted $F_0^{ll}(\epsilon)$ function and the data for the l^+l^- channel. The theoretical prediction is normalized to the number of events. The hatched histogram shows the predicted τ background events.

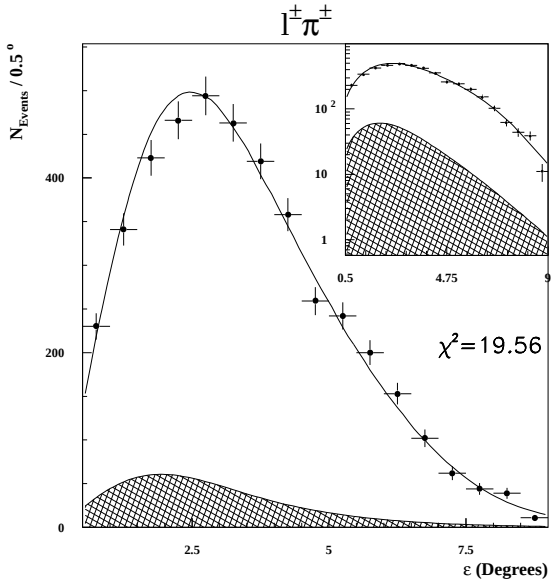

Figure 5.15: Comparison of the predicted $F_0^{l\pi}(\epsilon)$ function and the data for the $l^{\pm}\pi^{\mp}$ channel. The theoretical prediction is normalized to the number of events. The hatched histogram shows the predicted τ background events.

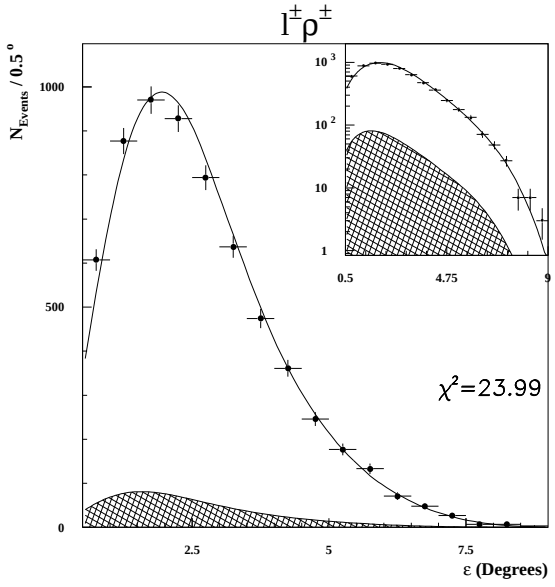

Figure 5.16: Comparison of the predicted $F_0^{l\rho}(\epsilon)$ function and the data for the $l^{\pm}\rho^{\mp}$ channel. The theoretical prediction is normalized to the number of events. The hatched histogram shows the predicted τ background events.

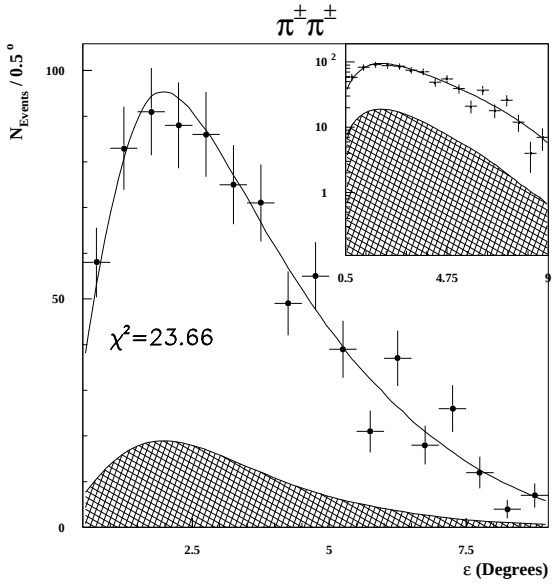

Figure 5.17: Comparison of the predicted $F_0^{\pi\pi}(\epsilon)$ function and the data for the $\pi^{\pm}\pi^{\mp}$ channel. The theoretical prediction is normalized to the number of events. The hatched histogram shows the predicted τ background events.

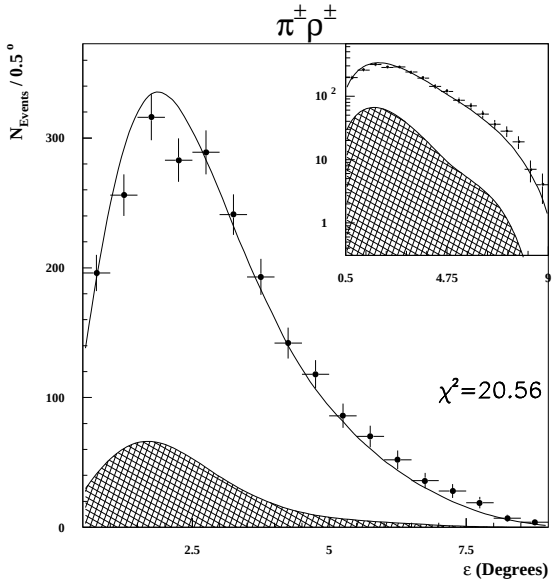

Figure 5.18: Comparison of the predicted $F_0^{\pi\rho}(\epsilon)$ function and the data for the $\rho^{\pm}\pi^{\mp}$ channel. The theoretical prediction is normalized to the number of events. The hatched histogram shows the predicted τ background events.

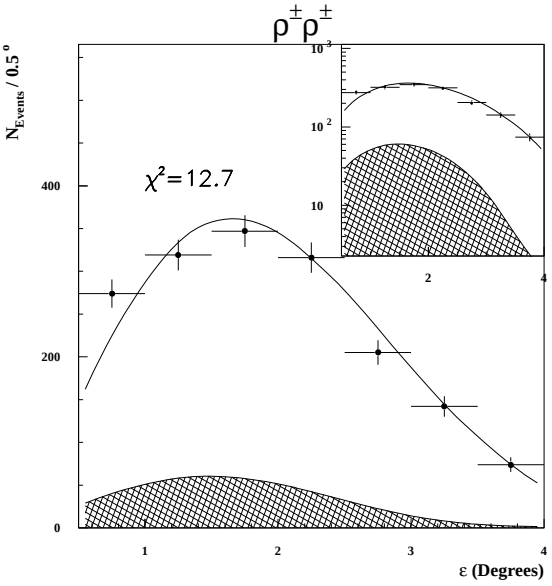

Figure 5.19: Comparison of the computed $F_0^{\rho\rho}(\epsilon)$ function and the data for the $\rho^{\pm}\rho^{\mp}$ channel. The theoretical prediction is normalized to the number of events. The hatched histogram shows the predicted τ background events.

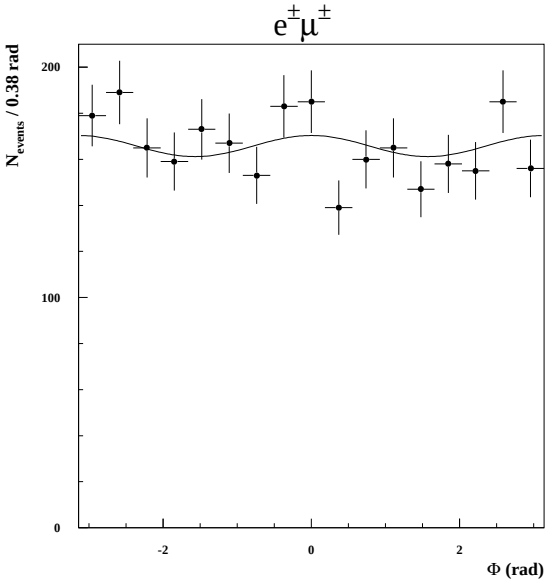

Figure 5.20: Number of events versus the aplanarity angle, ϕ (solid points) for the l^+l^- channel. The curve shows the Standard Model prediction normalized to the total number of events

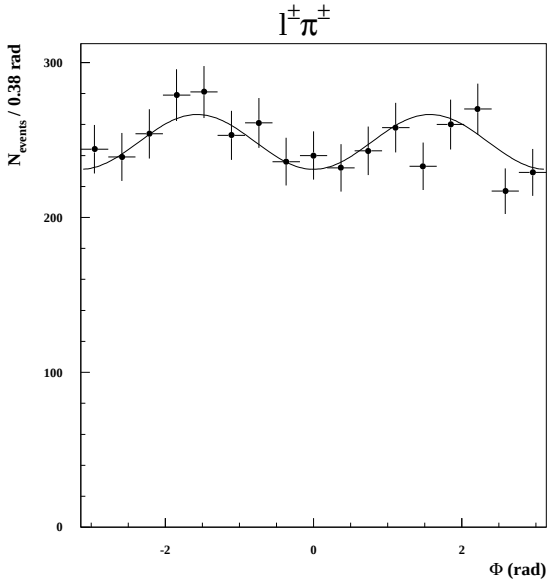

Figure 5.21: Number of events versus the aplanarity angle, ϕ (solid points) for the $l^{\pm}\pi^{\mp}$ channel. The curve shows the Standard Model prediction normalized to the total number of events

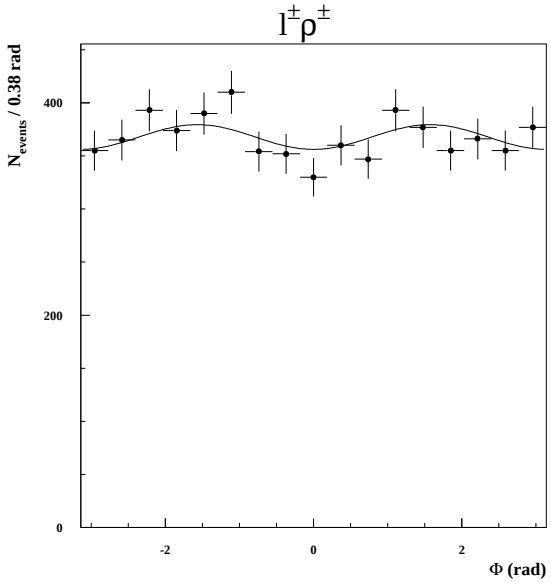

Figure 5.22: Number of events versus the aplanarity angle, ϕ (solid points) for the $l^{\pm}\rho^{\mp}$ channel. The curve shows the Standard Model prediction normalized to the total number of events

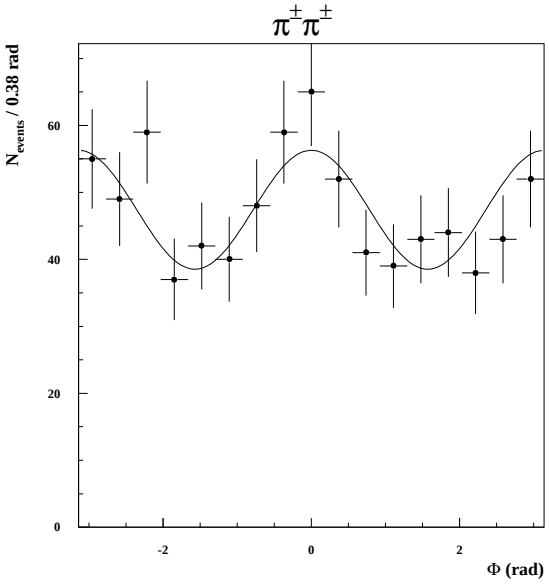

Figure 5.23: Number of events versus the aplanarity angle, ϕ (solid points) for the $\pi^+\pi^-$ channel. The curve shows the Standard Model prediction normalized to the total number of events

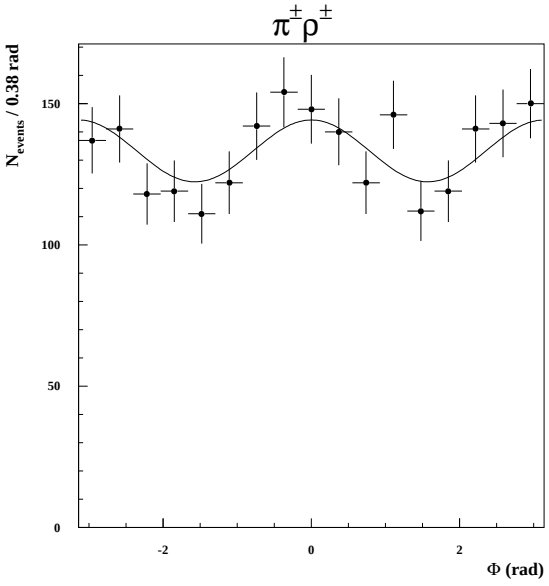

Figure 5.24: Number of events versus the aplanarity angle, ϕ (solid points) for the $\pi^{\mp}\rho^{\pm}$ channel. The curve shows the Standard Model prediction normalized to the total number of events

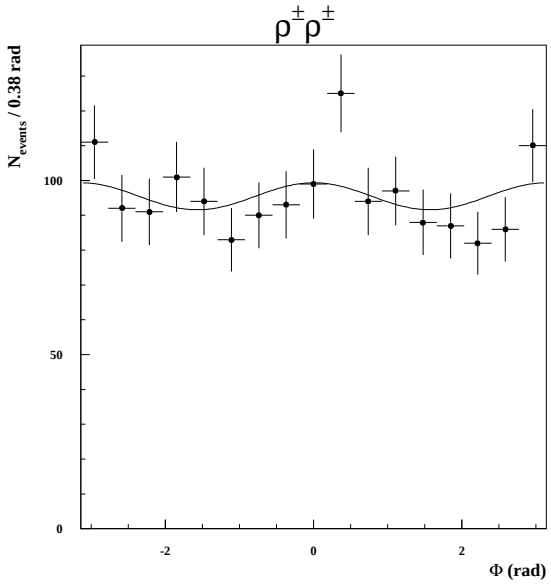

Figure 5.25: Number of events versus the aplanarity angle, ϕ (solid points) for the $\rho^+\rho^-$ channel. The curve shows the Standard Model prediction normalized to the total number of events

Chapter 6

Systematic Errors

The measurement of the transverse spin correlations A_{TT} and A_{TN} relies on the understanding of the physical parameters of the theory and the detector response. Any uncertainty in the input parameter of the theory, discrepancy between data and Monte Carlo or systematic effect of the detector can lead to systematic errors in the transverse spin correlations that should be estimated.

The input from the Monte Carlo consists of the mixing matrix between the different τ decay channels, the computation of the non-τ background and the estimation of the bias present in decay channels containing ρ's. The errors from the finite statistics of the Monte Carlo and the possible discrepancies between the Monte Carlo and the data are included as systematic uncertainties.

The uncertainties in the Standard Model parameters and on the τ decay branching ratios used when fitting the cross section are also considered as systematic errors.

Additional systematic errors are computed for the treatment of the Initial State Radiation correction.

The systematic uncertainties due to the angular smearing are also computed to estimate the detector effects on the measurements.

Most of the time, the mean value of the transverse spin correlations does not change due to the effects described above. It is just the statistical error of the measurements which does change. In those cases the systematic uncertainties are computed under the assumption that the change in the statistical errors are due

SM. parameter	W.A. value [16]	$\sigma_{A_{TT}}$	$\sigma_{A_{TN}}$
$\sin^2\theta_w$	0.2315 ± 0.0008	0.0004	0.0001
M_{Z^0}	$91.187 \pm 0.007 \mathrm{GeV/c^2}$	< 0.0001	0.0001
Γ_{Z^0}	$2.490 \pm 0.007 \mathrm{GeV/c^2}$	< 0.0001	0.0001
Total		0.0004	0.0002

Table 6.1: Systematics from the Standard Model parameters.

to a systematic uncertainties,

$$\sigma^2_{new} = \sigma^2_{old} + \sigma^2_{systematic} \tag{6.1}$$

6.1 Standard Model Parameters

The $\sin^2\theta_{\mathrm{W}}$, the Z^0 width (Γ_{Z^0}) and the Z^0 mass (M_{Z^0}) parameters are used to compute the fitted cross section. The world average values for these parameters are shown in Table 6.1. The uncertainties in the experimental values of these parameters are propagated to compute the systematic errors that are shown in Table 6.1. The systematic errors, computed under the assumption of eq. 6.1, are negligible for each parameter.

6.2 Branching Ratio systematic errors

The branching ratios are included in the analysis in two different ways. First of all the mixing matrix might be corrected by the difference between the Monte Carlo and the World Average values. The branching ratios experimental errors dominate the uncertainty in the correction. The second contribution of the branching ratios is due to the fact that the $\pi^{\pm}$ and $K^{\pm}$ are not distinguished in the analysis, and

τ decay channel	W.A. value [16]	MC Correction factor	$\sigma_{A_{TT}}$	$\sigma_{A_{TN}}$
$e^{\pm} + \mu^{\pm}$	35.18 ± 0.13	0.994 ± 0.008	0.001	0.001
$\pi^{\pm} + K^{\pm}$	12.01 ± 0.16	0.959 ± 0.013	0.006	0.006
$\rho^{\pm}$	25.24 ± 0.16	1.0382 ± 0.0066	0.003	0.003
$\pi\pi^0\pi^0$, $n\pi/K$	28.27 ± 0.22	1.0382 ± 0.0066	0.002	0.002
Total			0.009	0.009

Table 6.2: Systematics from the uncertainty in the Branching Ratios.

therefore the $Q_i(\epsilon)$ (i=1,3) functions are corrected by the relative branching fraction of K and π, see section 5.1.3.

The experimental values for the different τ decay branching ratios are shown in Table 6.2, where the correction factors for the mixing matrix and their errors are also shown. The systematic errors have been computed following the criteria described in eq. 6.1. These systematic errors are negligible compared with the statistical error.

The proper mixture of $\pi^{\pm}$'s and $K^{\pm}$'s used to computed the $Q_i(\epsilon)$ functions are computed from the world average values of the corresponding branching ratios. The uncertainties in both values are used to compute the systematic uncertainties. These values are presented in Table 6.3.

6.3 ρ asymmetry correction

The systematic uncertainties from the correction applied to the rho asymmetry reconstruction are computed from the Monte Carlo itself. The reconstruction uncertainties from the Monte Carlo are added quadratically with the statistical errors of each affected channel. The systematic error is then computed like the quadratic

$BR(\pi^{\pm})$ [16]	$BR(K^{\pm})$ [16]	$\sigma_{A_{TT}}$	$\sigma_{A_{TN}}$
$11.31 \pm 0.15\%$	$0.71 \pm 0.05\%$	0.002	< 0.001

Table 6.3: Systematics from the π/k mixing uncertainties.

$\sigma_{A_{TT}}$	$\sigma_{A_{TN}}$
0.039	0.040

Table 6.4: Systematics from the Monte Carlo correction to the ρ reconstruction asymmetry.

difference between the error obtained before and after applying the correction. The systematic errors are shown in Table 6.4 for the two transverse spin correlations. The minimum distance from a γ of a π^0 and the $\pi^{\pm}$ track extrapolation from a ρ decay into the electromagnetic calorimeter is compared between data and Monte Carlo in figure 5.2. The agreement is good and consequently no systematic error from the modelization of the asymmetry in the Monte Carlo is expected.

6.4 Non-τ background

The non-τ background is computed assuming that the number of events is equal to the one predicted by the Monte Carlo, Table 6.5. A number of events equal to the predicted background is subtracted from the data sample, the systematic error is computed as the difference between the correlations measured with and without the subtraction of the fake events. The comparison between data and the $e^+e^-/\mu^+\mu^-$ MC for the acollinearity and aplanarity angles are shown at Fig.6.4. The check is done by enriching the background in the control data sample with background events by means of the following cuts,

- events identified to be $l^{\pm}\pi^{\mp}$,
- and the total event energy larger 80 GeV.

These cuts anti-select the events we used in the likelihood fit. The agreement between the data and the Monte Carlo is good enough, as shown in figure 6.4, to justify the use of the Monte Carlo distribution to compute the systematic errors from the non-τ background.

Channel	$e^{\pm}\mu^{\mp}$	$l^{\pm}\pi^{\mp}$	$l^{\pm}\rho^{\mp}$	$\pi^{\pm}\pi^{\mp}$	$\pi^{\pm}\rho^{\mp}$	$\rho^{\pm}\rho^{\mp}$
Data	2818	4229	6253	806	2265	1623
e^+e^-	0.0	5.6 ± 2.0	6.3 ± 2.1	0.0	0.0	0.0
$\mu^+\mu^-$	0.51 ± 0.36	5.6 ± 1.2	1.0 ± 0.5	$.26 \pm .26$	0.0	0.0
total	0.51 ± 0.36	11.2 ± 2.3	7.3 ± 2.2	$.26 \pm .26$	0.0	0.0

Table 6.5: Number of events from non-τ contamination computed with the Monte Carlo.

The likelihood is minimized removing the sample of non-τ background events predicted by the Monte Carlo,

$$\mathcal{L} = \mathcal{L}_{data} + \sum_{i=1}^{N_{MC}} \ln\left(\frac{d\sigma_{corr}}{d\epsilon\ d\theta\ d\phi}(\epsilon_{MC}, \phi_{MC}, \theta_{MC}; A_{TT}, A_{ATN})\right), \qquad (6.2)$$

where the polar (θ_1^{MC}), the acollinearity (ϵ_{MC}) and the aplanarity (ϕ_{MC}) angles of the background events are obtained from the Monte Carlo events passing the selection cuts. The values multiplying the A_{TT} and A_{TN} parameters are taken in absolute value, defining the new angular distribution σ_{corr}, which overestimates the contribution from the non-τ background. The systematic errors shown in Table 6.6 are computed as the difference between the transverse spin correlations with and without the non-τ background correction. The statistic of the sample has been modified after the background subtraction and therefore the extraction of the systematic errors described in equation 6.1 cannot be applied.

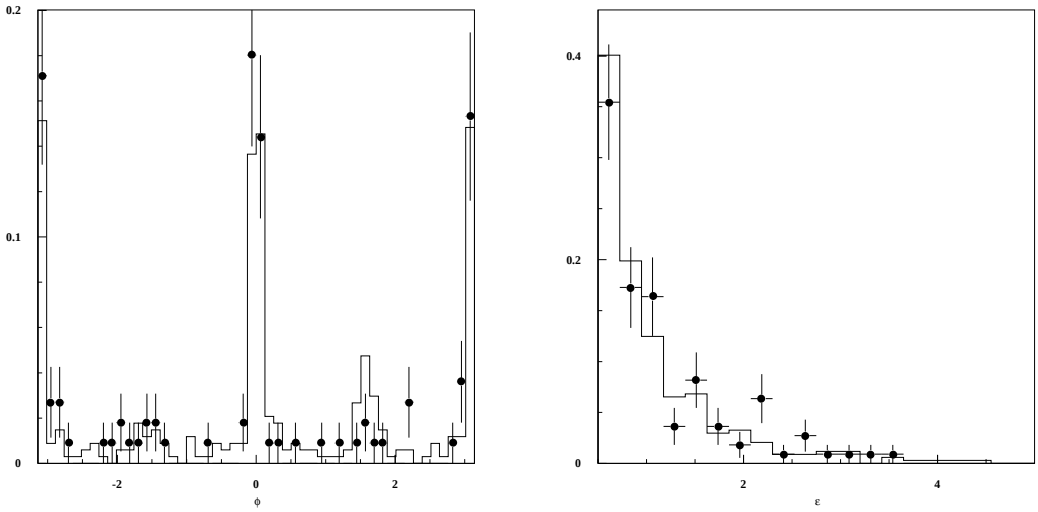

a) Aplanarity angle. b) Acollinearity angle.

Figure 6.1: Comparison between data (points with error bars) and the Monte Carlo for the e^+e^- and $\mu^+\mu^-$ background for the decay channel $l^{\pm}\pi^{\mp}$. The background is enhance selecting the events with $\epsilon > 0.5^o$ and $E_{tot} > 80.0$ GeV.

$\sigma_{A_{TT}}$	$\sigma_{A_{TN}}$
0.020	0.007

Table 6.6: Systematics from the non-τ background.

$\sigma_{A_{TT}}$	$\sigma_{A_{TN}}$
0.014	0.014

Table 6.7: Systematics from the mixing matrix statistics.

6.5 τ background estimation

The systematic error from the τ background estimation has two contributions: the finite statistic of the Monte Carlo used to compute the mixing matrix, see Table 4.2, and the uncertainties in the τ decay identification which is smaller than the Monte Carlo statistic contribution and is not considered.

The systematic error from the Monte Carlo statistic is computed changing the central value of the mixing matrix. The effect is enhanced by moving the background and the signal mean value in the opposite sense. The resulting systematic, computed like the quadratic difference between the statistical errors as it is described in equation 6.1, is shown at Table 6.7.

6.6 Smearing of the polar and the azimuthal angles

To estimate the error from the uncertainty in the polar and azimuthal angles, the likelihood fit is done convolving the cross-section with the smearing of the polar and the azimuthal angles. The angular smearing has been computed from the differences between the reconstructed and the generated Monte Carlo angles. The differences have been parametrized by three gaussians to take into account the long tails of the distributions. Figs. 6.2, 6.3, 6.4, 6.5, 6.6 and 6.7 show the Monte Carlo predictions and the parametrizations used for the cross section convolution.

The systematic errors are quoted as the quadratic differences between the variation of the statistical errors as described in equation 6.1. The systematic errors induced in the two transverse spin correlations are shown in Table 6.8. The values

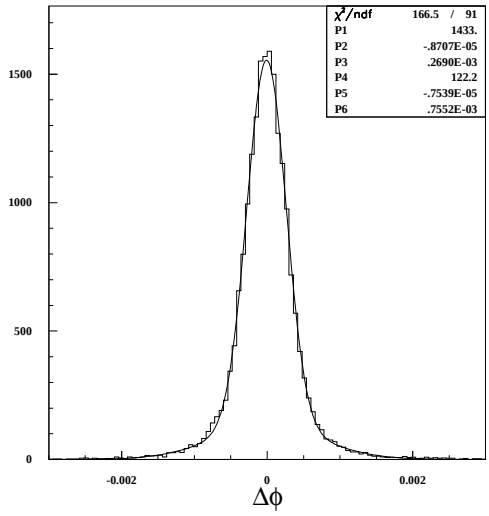

Figure 6.2: Distribution of the difference between generated and the reconstructed ϕ angle predicted by the Monte Carlo for the π. The parametrization comes from a three gaussian fit to the distribution.

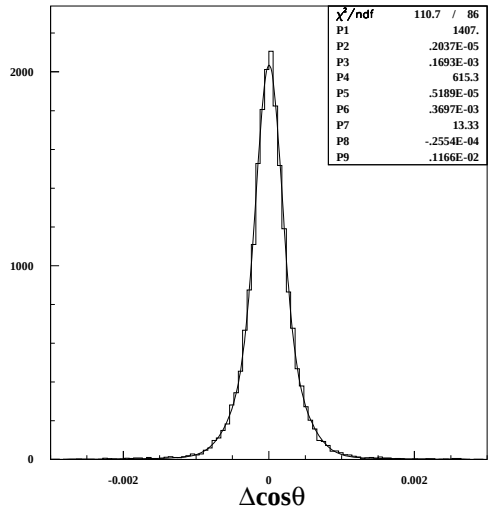

Figure 6.3: Distribution of the difference between generated and the reconstructed $\cos\theta$ predicted by the Monte Carlo for the π. The parametrization comes from a three gaussian fit to the distribution.

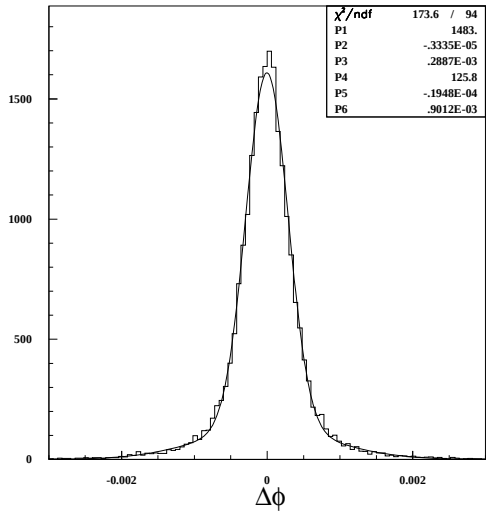

Figure 6.4: Distribution of the difference between generated and the reconstructed ϕ angles predicted by the Monte Carlo for the lepton. The parametrization comes from a three gaussian fit to the distribution.

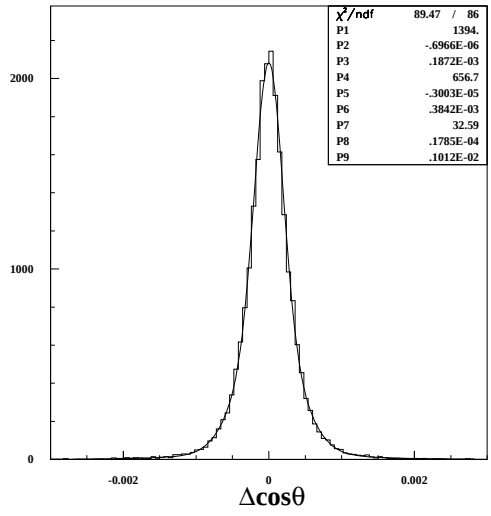

Figure 6.5: Distribution of the difference between generated and the reconstructed $\cos\theta$ predicted by the Monte Carlo for the lepton. The parametrization comes from a three gaussian fit to the distribution.

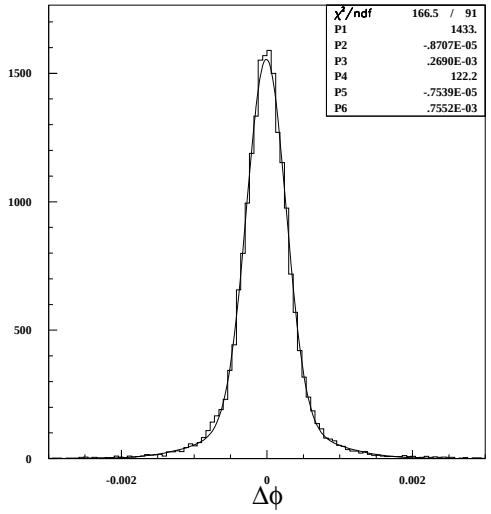

Figure 6.6: Distribution of the difference between generated and the reconstructed ϕ angle predicted by the Monte Carlo for the ρ. The parametrization comes from a three gaussian fit to the distribution.

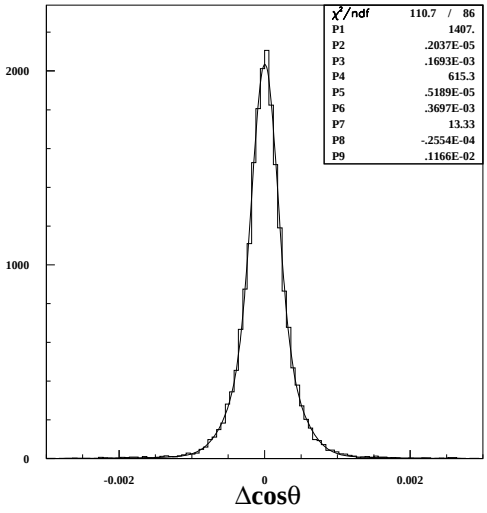

Figure 6.7: Distribution of the difference between generated and the reconstructed $\cos\theta$ predicted by the Monte Carlo for the ρ. The parametrization comes from a three gaussian fit to the distribution.

are negligible with respect to the statistical errors, and therefore no additional impact from the deficient description of this effect from the Monte Carlo is expected.

6.7 Initial State radiation

The systematic uncertainties from the the correction applied to the Initial State Radiation have different contributions. The ISR modelization main uncertainties come from the assumption of the photon radiation parallel to the beam direction,

$\sigma_{A_{TT}}$	$\sigma_{A_{TN}}$
0.003	0.003

Table 6.8: Systematics from the smearing of the polar and azimuthal angles.

Source	$\sigma_{A_{TT}}$	$\sigma_{A_{TN}}$
γ polar angle	0.002	0.001
ISR $A_{(x_{max}=1.0)} - A_{(x_{min}=0.2)}$	≈ 0	≈ 0

Table 6.9: Systematics from the modelization of the Initial State Radiation.

and from the change in the $Q_i(\epsilon)$ functions with the center of mass energy.

6.7.1 Angle of the ISR photons

The systematic errors are estimated as the difference between the values obtained with the cosine of the angle of the ISR photons fixed to 1.0 and 0.95 (maximum angle of the ISR photons seen by the ALEPH detector). The emission probability is peaked at 1.0 and therefore the above interval gives an upper limit of the systematic errors, which are nevertheless negligible. The quoted errors for the transverse-transverse and transverse-normal spin correlations are shown at Table 6.9.

6.7.2 Variation of the $Q_i(\epsilon)$ functions with the center of mass energy

The $Q_i(\epsilon)$ functions used in the fit are computed at the Z^0 center of mass energy, and they are corrected by a kinematical factor for the ISR events,

$$(180^\circ - \epsilon') \;=\; (180^\circ - \epsilon)\sqrt{1-x} \tag{6.3}$$

where x is the fraction of the center of mass energy carried by the radiated photon.

The systematic errors are the difference between the values of the transverse spin correlations computed for $x_{max} = 0.2$ and $x_{max} = 1.0 - \delta$. The systematic errors are shown at Table 6.9.

$\sigma_{A_{TT}}$	$\sigma_{A_{TN}}$
- - -	0.002

Table 6.10: Systematics from the d_τ dipole form factor.

6.8 Dipole form factors

The transverse spin correlations are independent [31] of the $\tilde{d}_\tau$ dipole form factors, see [30]. However, it is shown in Appendix D that one of the two transverse spin polarizations, and one of the two transverse-longitudinal spin correlations contribute to the observable from which the A_{TN} is measured. The limit of the dipole form factor value already published by the ALEPH and OPAL collaborations [30] has been used to estimate the uncertainty induced in A_{TN}, which is shown in Table 6.10.

Source	ΔA_{TT}	ΔA_{TN}
Mixing	0.014	0.014
$\sin^2_{eff}(\theta_w), M_{Z^0}, \Gamma_{Z^0}$	≈ 0.0	≈ 0.0
$BR(\tau \to K\nu)/BR(\tau \to \pi\nu)$	0.002	≈ 0.0
Angle smearing	0.003	0.003
Non-τ background	0.020	0.007
ISR angular dependence	0.002	0.001
ISR $A_{x_{max}=1.0} - A_{x_{max}=0.2}$	≈ 0.0	≈ 0.0
ρ asymmetry	0.039	0.040
τ decay branching ratios	0.009	0.009
dipole form factor d_τ	- - -	0.002
Total	0.05	0.04

Table 6.11: Systematic uncertainties on the fitted transverse spin correlations.

6.9 Summary of the main systematic errors

The main systematic errors are summarized at Table 6.11. As it is shown the main contribution to the final errors is coming from the ρ reconstruction asymmetry, which is computed based on the Monte Carlo. Other important contributions are coming from the Monte Carlo statistic for the non-τ background and the experimental uncertainties in the τ decay branching ratios.

Chapter 7

Electroweak parameters from the transverse spin correlations

7.1 A_{TT} spin correlation

The definition of the transverse-transverse spin correlation as a function of the vector and axial vector Z-$\tau^+\tau^-$ couplings,

$$A_{TT} = \frac{|a_\tau|^2 - |v_\tau|^2}{|a_\tau|^2 + |v_\tau|^2}, \tag{7.1}$$

clearly indicates that its value depends on which of these two couplings is larger. The value of the A_{TT} spin correlation, 1.06 $\pm$ 0.14, clearly indicates that the axial vector coupling is larger than the vector coupling. The measured spin correlation is 15 σ away from -1, i.e. the purely vector coupling. This is the first time this prediction of the Standard Model theory is checked from purely "weak" contributions in e^+e^- collisions. Traditionally this asymmetry between the vector and the axial vector couplings is inferred from $Z^0-\gamma$ interference, which is a phenomena that mixes "weak" and "electromagnetic" effects. Fig. 7.1 displays the region in the (v_τ, a_τ) plane (shaded area) allowed by this measurement.

Although the sensitivity to the weak mixing parameter, $\sin^2\theta_W^{eff}$, cannot compete with the values obtained from the longitudinal τ spin polarization and correlation measurements, a limit in its value can be inferred from the A_{TT} spin correlation, which depends on $\sin^2\theta_W^{eff}$ as,

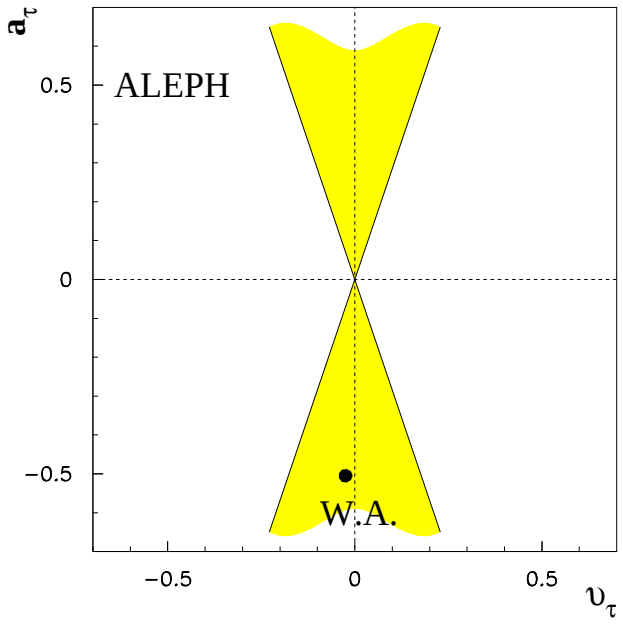

Figure 7.1: 95% C.L. allowed region (shaded) for the ν_τ and a_τ couplings. The point shows the world average (W.A.) values for the vector and axial vector couplings.

$$A_{TT} = \frac{|-1/2|^2 - |-1/2 + 2\sin^2\theta_W^{eff}|^2}{|-1/2|^2 + |-1/2 + 2\sin^2\theta_W^{eff}|^2}.$$

Due to the special definition of the A_{TT} parameter, values greater than one are not physically allowed. This fact constrains the information to be extracted from the A_{TT} correlation. The measured value for the A_{TT} correlation falls outside the boundary of the physical region. For that reason only a minimum limit on the $\sin^2\theta_W^{eff}$ can be extracted,

$$\sin^2\theta_W^{eff} > 0.17 \;\; C.L. = 95\%$$

in agreement with the actual World Average value, $\sin^2\theta_{\rm W}^{eff} = 0.2315 \pm 0.0008$[16].

7.2 A_{TN} spin correlation

The definition of the transverse-normal spin correlation parameter in terms of the $Z^0 - \tau^+\tau^-$ couplings, as it is shown in section 2.36, is

$$A_{TN} = \frac{-2\Im(v_\tau a_\tau^*)}{|a_\tau|^2 + |v_\tau|^2}.$$

The T-odd parameter A_{TN} carries information about the imaginary part of the Z^0-$\tau^+\tau^-$ couplings as shown in section 2.38,

$$\tan(\Phi_{v_f} - \Phi_{a_f}) = \frac{D_2}{-D_0} = \frac{A_{TN}}{P_\tau}$$

The World Average value for the τ longitudinal polarization is $P_Z = -0.142 \pm 0.007$ [29], and it is combined with the measured transverse spin correlation $A_{TN} = 0.08 \pm 0.14$ to obtain a value of the relative phase between the axial and vector couplings:

$$\tan(\Phi_{v_f} - \Phi_{a_f}) = 0.56 \pm 0.98$$

The phases Φ_{v_f} and Φ_{a_f} have been defined in chapter 2. The result is compatible with a purely real couplings, as predicted by the Standard Model.

Appendix A

$Q_i(\epsilon)$ functions

The inclusion of the spin and the mass of the final state particles during the integration of (2.51) is described in many places [14, 15, 17]. Although this inclusion is feasible in analytic calculations, there is still some effects that cannot be easily implemented, like the finite mass width of some hadronic channels (ρ, a_1, ...) and the γ radiation in the τ decays. On the other hand, some hadronic τ decays involving multi-pion states cannot be computed easily and should be considered at the experimental level as the most important contribution to the background. There are however some Monte Carlo programs describing the τ decay that include all these effects. One of them, TAUOLA [11], has been tested in the LEP experiments reproducing quite well the experimental data. This Monte Carlo can be thus used [17] to integrate the (2.51) cross section, obtaining the $Q_i(\epsilon)$ functions for each $\tau^+\tau^-$ decay channel.

The terms multiplying the $F_i(s)$ and $G_i(s)$ in (2.22) can be easily related with the terms in (2.51):

$$\begin{aligned}
Q_1(\epsilon)(1+\cos^2\theta_1) &\rightarrow (1 - s^*_{1z}s^*_{2z})(1+\cos^2\theta) \\
Q_2(\epsilon)(1+\cos^2\theta_1) &\rightarrow (s^*_{1z} + s^*_{2z})(1+\cos^2\theta) \\
Q_3(\epsilon)\sin^2\theta_1 &\rightarrow (s^*_{1y}s^*_{2y} - s^*_{1x}s^*_{2x})\sin^2\theta \quad \text{and} \quad (s^*_{1y}s^*_{2x} + s^*_{1x}s^*_{2y})\sin^2\theta
\end{aligned} \tag{A.1}$$

The $Q_n^{ij}(\epsilon)$ functions turn out to be:

$$
\begin{aligned}
\frac{dQ_1^{ij}(\epsilon)}{d\epsilon} &= \int d\cos\theta dq_1 dq_2 d\theta_1 \; d\phi \; d\chi \; d\psi d\hat{s}_1^* d\hat{s}_2^* \frac{\partial(\vec{q}_1^*, \vec{q}_2^*, \theta)}{\partial(q_1, q_2, \theta_1, \epsilon, \phi, \chi, \psi)} \\
&\quad \frac{d\Gamma(\hat{s}_1^*, \vec{q}_1^*)}{d\vec{q}_1^*} \frac{d\Gamma(\hat{s}_2^*, \vec{q}_2^*)}{d\vec{q}_2^*} (1 - s_{1z}^* s_{2z}^*) \frac{1 + \cos^2\theta}{1 + \cos^2\theta_1} \\
\frac{dQ_2^{ij}(\epsilon)}{d\epsilon} &= \int d\cos\theta dq_1 dq_2 d\theta_1 \; d\phi \; d\chi \; d\psi d\hat{s}_1^* d\hat{s}_2^* \frac{\partial(\vec{q}_1^*, \vec{q}_2^*, \theta)}{\partial(q_1, q_2, \theta_1, \epsilon, \phi, \chi, \psi)} \\
&\quad \frac{d\Gamma(\hat{s}_1^*, \vec{q}_1^*)}{d\vec{q}_1^*} \frac{d\Gamma(\hat{s}_2^*, \vec{q}_2^*)}{d\vec{q}_2^*} (s_{1z}^* - s_{2z}^*) \frac{1 + \cos^2\theta}{1 + \cos^2\theta_1} \\
\frac{dQ_3^{ij}(\epsilon)}{d\epsilon} &= \int d\cos\theta dq_1 dq_2 d\theta_1 \; d\phi \; d\chi \; d\psi d\hat{s}_1^* d\hat{s}_2^* \frac{\partial(\vec{q}_1^*, \vec{q}_2^*, \theta)}{\partial(q_1, q_2, \theta_1, \epsilon, \phi, \chi, \psi)} \\
&\quad \frac{d\Gamma(\hat{s}_1^*, \vec{q}_1^*)}{d\vec{q}_1^*} \frac{d\Gamma(\hat{s}_2^*, \vec{q}_2^*)}{d\vec{q}_2^*} (s_{1y}^* s_{2y}^* - s_{1x}^* s_{2x}^*) \frac{\sin^2\theta}{\sin^2\theta_1} \frac{1}{\cos(2\phi)} \\
\frac{dQ_3^{ij}(\epsilon)}{d\epsilon} &= \int d\cos\theta dq_1 dq_2 d\theta_1 \; d\phi \; d\chi \; d\psi d\hat{s}_1^* d\hat{s}_2^* \frac{\partial(\vec{q}_1^*, \vec{q}_2^*, \theta)}{\partial(q_1, q_2, \theta_1, \epsilon, \phi, \chi, \psi)} \\
&\quad \frac{d\Gamma(\hat{s}_1^*, \vec{q}_1^*)}{d\vec{q}_1^*} \frac{d\Gamma(\hat{s}_2^*, \vec{q}_2^*)}{d\vec{q}_2^*} (s_{1y}^* s_{2x}^* + s_{1x}^* s_{2y}^*)) \frac{\sin^2\theta}{\sin^2\theta_1} \frac{1}{\sin(2\phi)}
\end{aligned}
\tag{A.2}
$$

where $d\Gamma(\hat{s}_2^*, \vec{q}_2^*)/d\vec{q}_2^*$ is the angular distribution of the τ decay product, $\vec{q}_i^*$, in the τ rest frame from an arbitrary polarization, $\hat{s}_i^*$ (2.5.1). The index ij runs for the considered $\tau^+\tau^-$ decay products.

An uniform $\tau^-\tau^+$ polar angle distribution is generated. For every τ lepton the spin polarization, $\hat{s}_i^*$, and the momenta of the τ decay products are generated by the TAUOLA Monte Carlo [11]. Base on those distributions the $Q_i(\epsilon)$ functions are computed numerically. The result of those integrations for several channels are shown in Fig. A.1, A.2 and A.3.

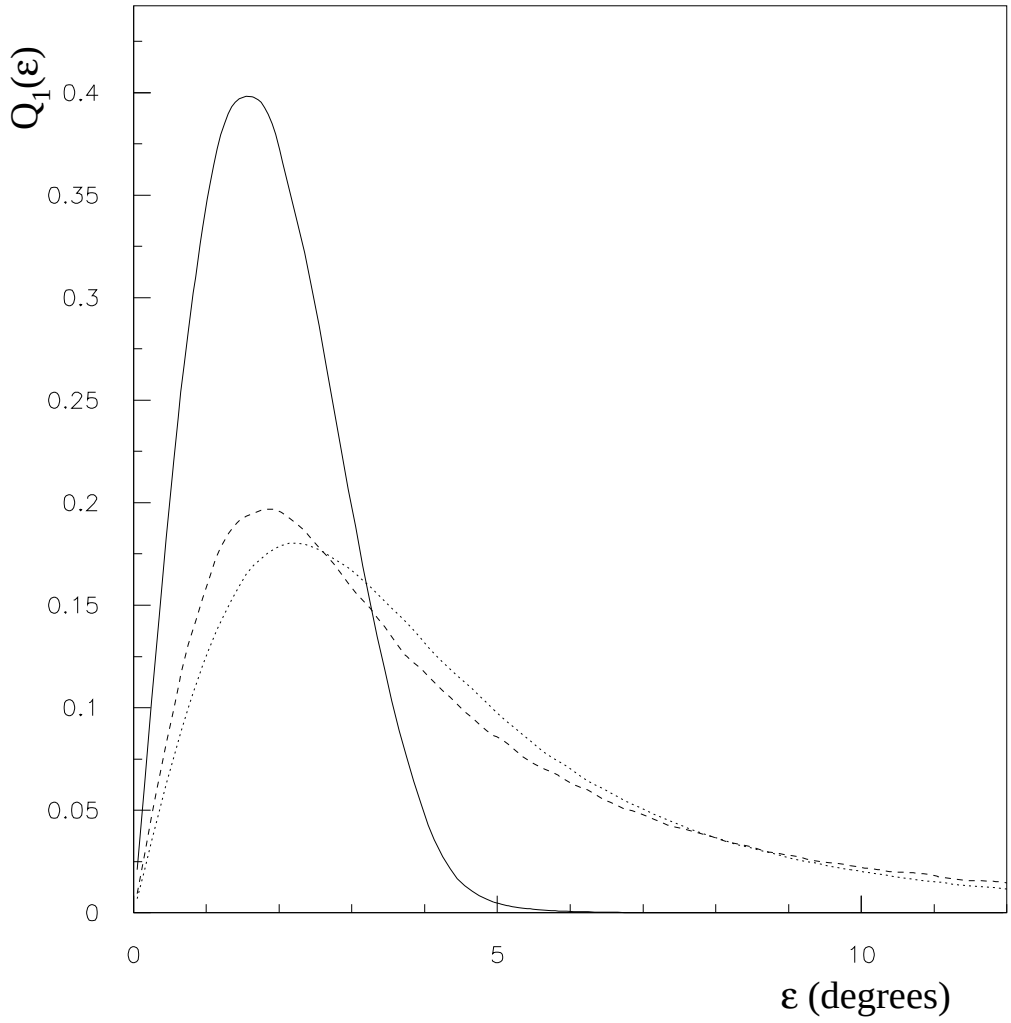

Figure A.1: $Q_1^{ij}(\epsilon)$ functions for the $\rho^-\rho^+$ (full line), $\pi^-\pi^+$ (dashed line) and l^+l^- (dotted line) decay channels.

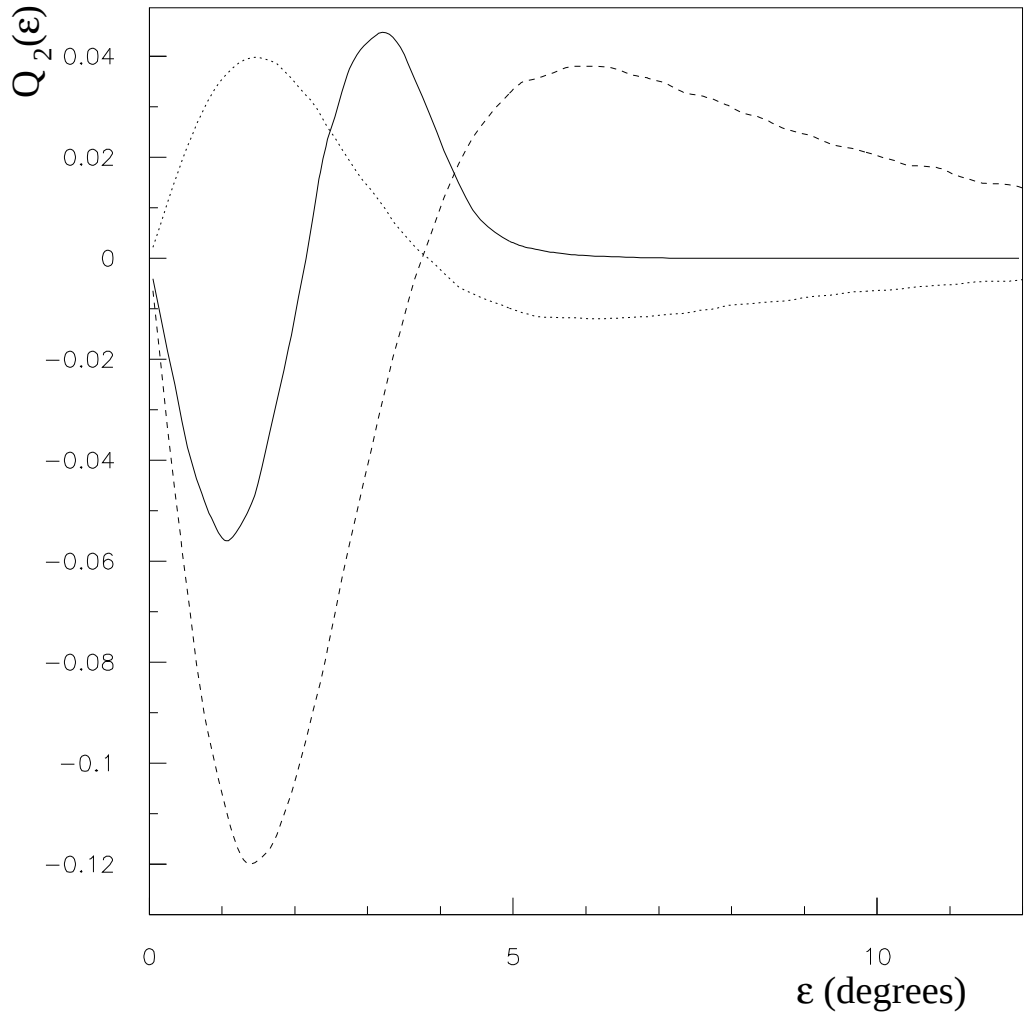

Figure A.2: $Q_2^{ij}(\epsilon)$ functions for the $\rho^-\rho^+$ (full line), $\pi^-\pi^+$ (dashed line), and l^+l^- (dotted line) decay channels.

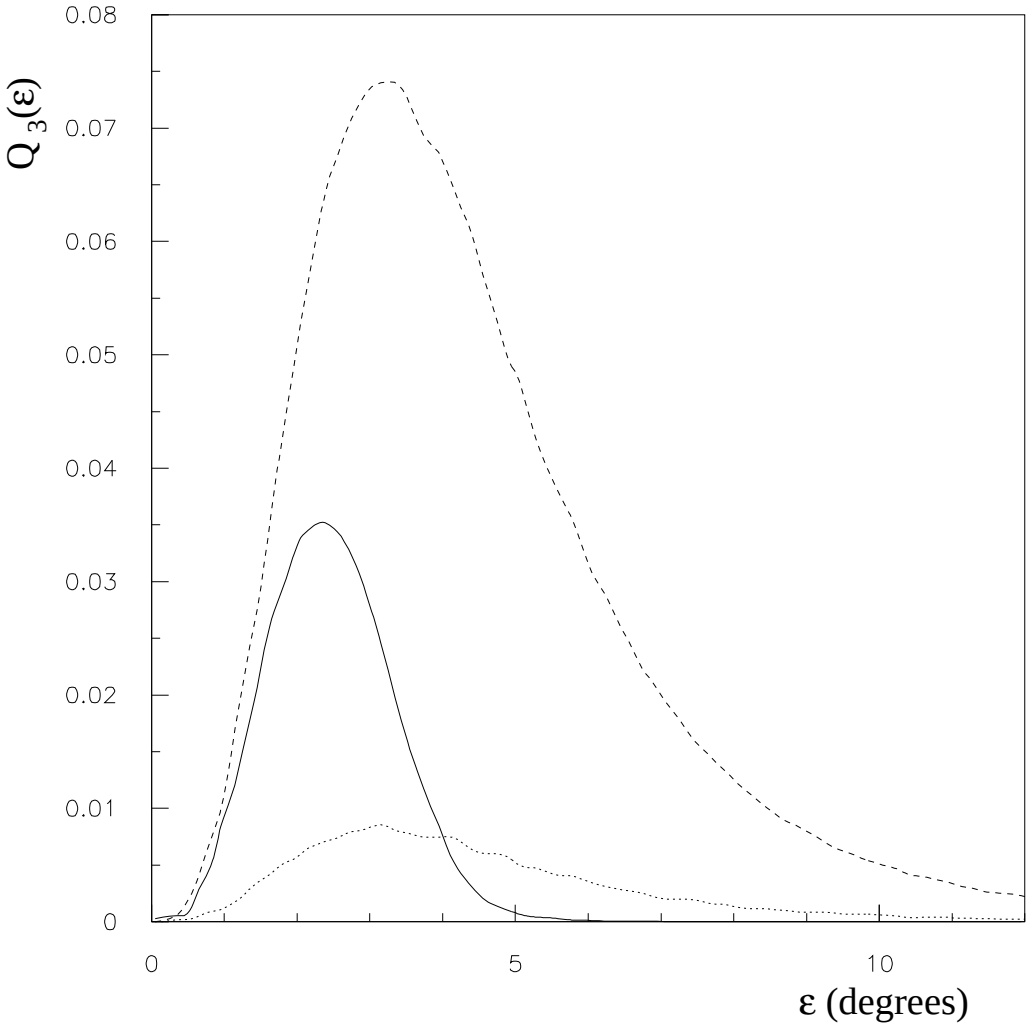

Figure A.3: $Q_3^{ij}(\epsilon)$ functions for the $\rho^-\rho^+$ (full line), $\pi^-\pi^+$ (dashed line), and l^+l^- (dotted line) decay channels.

Appendix B

Channel sensitivity to the spin correlations.

As in the well known longitudinal polarization studies, the τ spin vectors are not directly measurable, but the τ decay products can be used as spin analyzers. The transverse spin correlations give raise to angular correlations of the decay products. The correlation between the spin and the τ decay product is weighted by the polarization parameter α_i which depends on the particular decay channel, see section 2.5.1. This polarization parameter appear in the final cross-section, eq. 2.51, multiplying the spin correlation observables $F_2(s)$ and $G_2(s)$, and therefore reducing the sensitivity to measure those spin correlations. The sensitivity of the different analyzed $\tau^+\tau^-$ decay channels are shown in table B.1.

Channel	Sensitivity ($\alpha_i\alpha_j$)
$e^{\pm}\mu^{\mp}$	0.11
$l^{\pm}\pi^{\mp}$	-0.33
$l^{\pm}\rho^{\mp}$	-0.15
$\pi^{\pm}\pi^{\mp}$	1.00
$\pi^{\pm}\rho^{\mp}$	0.46
$\rho^{\pm}\rho^{\mp}$	0.21

Table B.1: Sensitivity to the transverse spin correlation for each considered channel.

The fact that the polarization parameter of the leptonic decay is negative, eq. 2.42, leads to negative values of the sensitivity for non pure leptonic or hadronic

$\tau^+\tau^-$ decays. The data analysis should therefore distinguish between the different τ decay channels to avoid the cancellation of the sensitivities which would increase the statistical errors. A similar effect is present, although not so strongly, when mixing various hadronic decay channels.

Appendix C

The aplanarity angle

The definition of the aplanarity angle is

$$\phi \;=\; \arctan \frac{\frac{(\hat{p}_{d^-}\times\hat{p}_{d^+})\cdot\hat{p}_{beam}}{|\hat{p}_{d^-}\times\hat{p}_{d^+}|}}{\frac{(\hat{p}_{d^-}\times\hat{p}_{d^+}\times\hat{p}_{d^-})\cdot\hat{p}_{beam}}{|\hat{p}_{d^-}\times\hat{p}_{d^+}\times\hat{p}_{d^-}|}},$$

where $\hat{p}_{d^\pm}$ are the directions of the $\tau^\pm$ decay products in the laboratory rest frame,

$$\begin{aligned}\hat{p}_{d^-} &= (\sin\theta_1\cos\phi_1, \sin\theta_1\sin\phi_1, \cos\theta_1),\\ \hat{p}_{d^+} &= (\sin\theta_2\cos\phi_2, \sin\theta_2\sin\phi_2, \cos\theta_2).\end{aligned}$$

and $\hat{p}_{beam}$ is the beam direction in the same reference system,

$$\hat{p}_{beam} \;=\; (0,0,1).$$

The aplanarity angle as a function of these angles is given by the expression,

$$\phi \;=\; \arctan\left(\frac{\sin\theta_2\sin(\phi_1-\phi_2)}{\sin\theta_1\cos\theta_2-\cos\theta_1\sin\theta_2\cos(\phi_1-\phi_2)}\right)$$

The negative and positive decay products are almost back to back, and therefore the polar angles are related,

$$\sin\theta_1 \;\approx\; \sin\theta_2\ ,\ \cos\theta_1 \approx -\cos\theta_2.$$

Using these expresions, the expresion of the aplanarity angle can be simplified,

$$\phi \;=\; \arctan\frac{-\sqrt{2}\sin(\frac{\phi_1-\phi_2}{2})}{\cos\theta_1}$$

C.1 Symmetries

C.1.1 Charge conjugation: C

The charge conjugation swaps the positive and negative τ decays, $1 \leftrightarrow 2$. The difference in the aplanarity angle changes its sign and the polar angle of the negative decay turns to be the polar angle of the positive τ decay product,

$$\begin{aligned} \Delta\phi_i &\rightarrow -\Delta\phi_i \\ \cos\theta_1 &\rightarrow \cos\theta_2 = -\cos\theta_1. \end{aligned}$$

The aplanarity angle changes as,

$$\phi \rightarrow \phi + \pi \tag{C.1}$$

The two functions $\cos 2\phi$ and $\sin 2\phi$ remain the same under a rotation of π rad. of the aplanarity angle, and therefore both observables are then C-even.

C.1.2 Parity : P

The parity operator changes the polar and azimuthal angles as follows,

$$\begin{aligned} \phi_i &\rightarrow \phi_i + \pi \\ \cos\theta_i &\rightarrow -\cos\theta_i \end{aligned}$$

and therefore the aplanarity angle is modified as shown in Fig.C.1.

The $\cos 2\phi$ function is a P-even observable because it remains the same under the parity transformation shown in C.1.b. On the other hand, the $\sin 2\phi$ function is a P-odd observable because it changes the sign under the parity transformation as shown in C.1.c.

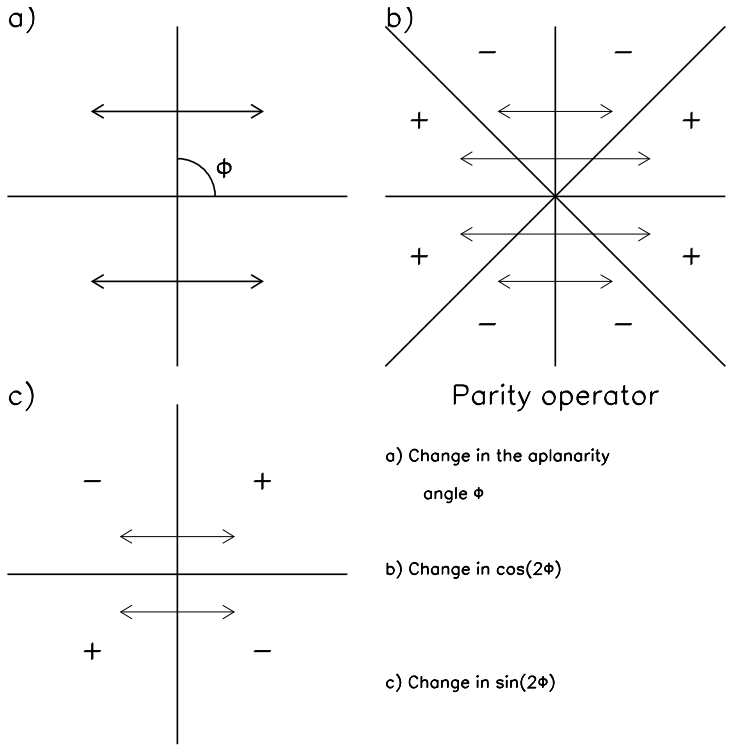

Figure C.1: The change in the aplanarity due to the parity operator.

Appendix D

Non transverse spin correlation contributions to the transverse spin observables

The difficulty to reconstruct the τ spin direction requires the use of the observables $\sin^2\theta_1 cos(2\phi)$ and $\sin^2\theta_1 sin(2\phi)$ in the transverse spin correlations measurements. But, other spin combinations different from the two transverse spin correlations can contribute to these observables. We checked the residual contributions of the different spin combinations to both transverse spin observables. Using the procedure described in [17], the contribution of the different spin combination has been computed for the most sensitive $\pi^+\pi^-$ channel. The integrals normalized with respect to the corresponding transverse spin correlations are computed as follows,

$$\begin{aligned}
I_i^{TT} &= \frac{\int w_i \sin^2\theta cos(2\phi) dLisp}{\int(-s_{1x}^* s_{2x}^* + s_{1y}^* s_{2y}^*)\sin^2\theta cos(2\phi) dLisp} \\
I_i^{TN} &= \frac{\int w_i \sin^2\theta sin(2\phi) dLisp}{\int(s_{1y}^* s_{2x}^* + s_{1x}^* s_{2y}^*)\sin^2\theta sin(2\phi) dLisp} \\
IC_i^{TT} &= \frac{\int w_i \sin\theta\cos\theta cos(2\phi) dLisp}{\int(-s_{1x}^* s_{2x}^* + s_{1y}^* s_{2y}^*)\sin^2\theta cos(2\phi) dLisp} \\
IC_i^{TN} &= \frac{\int w_i \sin\theta\cos\theta sin(2\phi) dLisp}{\int(s_{1y}^* s_{2x}^* + s_{1x}^* s_{2y}^*)\sin^2\theta sin(2\phi) dLisp}
\end{aligned} \tag{D.1}$$

where w_i are the different spin combinations, up to second order, between the spin components of both τ's. The w_i combinations and the results computed with the TAUOLA Monte Carlo describing the τ decay are shown in Table D.

w_i	IC_i^{TT}	IC_i^{TN}	I_i^{TT}	I_i^{TN}
$(1 + s_{1z}^* s_{2z}^*)$	0.0017 ± 0.0024	-0.0027 ± 0.0024	-0.0034 ± 0.0024	0.0006 ± 0.0024
$(1 - s_{1z}^* s_{2z}^*)$	0.0017 ± 0.0024	-0.0027 ± 0.0024	-0.0034 ± 0.0024	0.0006 ± 0.0024
$(s_{1z}^* + s_{2z}^*)$	-0.0025 ± 0.0024	0.0018 ± 0.0024	-0.0007 ± 0.0024	0.0003 ± 0.0024
$(s_{1z}^* - s_{2z}^*)$	0.0053 ± 0.0024	0.0002 ± 0.0024	-0.0045 ± 0.0024	0.0025 ± 0.0024
$(s_{1x}^* + s_{2x}^*)$	0.0013 ± 0.0024	0.0016 ± 0.0024	0.0020 ± 0.0024	-0.0007 ± 0.0024
$(s_{1x}^* - s_{2x}^*)$	0.0020 ± 0.0024	-0.0441 ± 0.0024	0.0071 ± 0.0024	-0.0003 ± 0.0024
$(s_{1y}^* + s_{2y}^*)$	-0.0083 ± 0.0024	-0.0001 ± 0.0024	-0.0046 ± 0.0024	-0.0037 ± 0.0024
$(s_{1y}^* - s_{2y}^*)$	0.0590 ± 0.0024	0.0018 ± 0.0024	-0.0011 ± 0.0024	-0.0025 ± 0.0024
$(s_{1y}^* s_{2z}^* + s_{2y}^* s_{1z}^*)$	-0.0390 ± 0.0024	-0.0005 ± 0.0024	-0.0034 ± 0.0024	-0.0021 ± 0.0024
$(s_{1y}^* s_{2z}^* - s_{2y}^* s_{1z}^*)$	0.0009 ± 0.0024	0.0006 ± 0.0024	-0.0015 ± 0.0024	-0.0015 ± 0.0024
$(s_{1x}^* s_{2z}^* + s_{2x}^* s_{1z}^*)$	0.0021 ± 0.0024	0.0295 ± 0.0024	-0.0055 ± 0.0024	-0.0014 ± 0.0024
$(s_{1x}^* s_{2\bar{z}}^* s_{2x}^* s_{1z}^*)$	-0.0028 ± 0.0024	0.0010 ± 0.0024	0.0039 ± 0.0024	-0.0009 ± 0.0024
$(s_{1y}^* s_{2y}^* + s_{1x}^* s_{2x}^*)$	0.0001 ± 0.0024	-0.0030 ± 0.0024	-0.0011 ± 0.0024	-0.0027 ± 0.0024
$(s_{1y}^* s_{2y}^* - s_{1x}^* s_{2x}^*)$	0.0015 ± 0.0024	-0.0021 ± 0.0024	1.00 (norm)	-0.0008 ± 0.0024
$(s_{1y}^* s_{2x}^* + s_{1y}^* s_{1y}^*)$	-0.0004 ± 0.0024	0.0026 ± 0.0024	0.0016 ± 0.0024	1.0 (norm)
$(s_{1y}^* s_{2x}^* - s_{1y}^* s_{1y}^*)$	0.0000 ± 0.0024	-0.0012 ± 0.0024	-0.0034 ± 0.0024	-0.0002 ± 0.0024

The only contribution different from zero is the transverse spin distribution, $IC^{TN}_{(s^*_{1x}-s^*_{2x})}$ and $IC^{TN}_{(s^*_{1x}s^*_{2z}+s^*_{2x}s^*_{1z})}$ which modifies the transverse-normal spin correlation, and $IC^{TT}_{(s^*_{1y}-s^*_{2y})}$ and $IC^{TT}_{(s^*_{1y}s^*_{2z}+s^*_{2y}s^*_{1z})}$, which contributes to the transverse-transverse spin correlation. According to [31], the anomalous coupling coefficients multiplying the previous terms are,

$$\begin{aligned} IC^{TN}_{(s^*_{1x}-s^*_{2x})} &\rightarrow 8a_\tau(a_e^2+\nu_e^2)\Re(\tilde{d}_\tau) \\ IC^{TN}_{(s^*_{1x}s^*_{2z}+s^*_{2x}s^*_{1z})} &\rightarrow 8a_\tau(a_e^2+\nu_e^2)\Im(m\nu_\tau+\mu_\tau) \\ IC^{TT}_{(s^*_{1y}-s^*_{2y})} &\rightarrow 8a_\tau(a_e^2+\nu_e^2)\Re(m\nu_\tau+\mu_\tau) \\ IC^{TT}_{(s^*_{1y}s^*_{2z}+s^*_{2y}s^*_{1z})} &\rightarrow 8a_\tau(a_e^2+\nu_e^2)\Im(\tilde{d}_\tau) \end{aligned} \tag{D.2}$$

where $\tilde{d}_\tau$ is the weak dipole form factor, μ_τ is the weak magnetic moment and $m=\frac{2m_\tau}{M_{Z^0}}$.

Bibliography

[1] ALEPH Collab. D.Camp *et al.*, Phys. Lett. **B265** (1991) 430.
ALEPH Collab. D.Buskulic *et al.*, Z.Phys. **69** (1996) 183.

[2] OPAL Collab. G.Alexander *et al.*, Phys. Lett. **B266** (1991) 201.
OPAL Collab. R. Akers *et al.*, Z.Phys. **C65** (1995) 1.

[3] L3 Collab., O. Adriani *et al.*, Phys.Lett. **B294** (1992) 466.
L3 Collab., O. Acciarri *et al.*, Phys.Lett. **B341** (1994) 245.

[4] DELPHI Collab., P.Abreu *et al.*, Phys.Lett. **B265** (1991) 430.

[5] F.Sánchez, Z.Wąs, Phys.Lett. **B351** (1995) 562.

[6] "First Evidence of transverse spin correlations in Z^0 Decays", DELPHI 95-111 PHYS 546

[7] J. Bernabéu, N. Rius and A. Pich, Phys.Lett. **B257** (1991) 219.

[8] Ricard Alemany Pantebre, "Tau Polarization from Angular Correlations", Ph.D. thesis, Universitat Autónoma de Barcelona, Institut de Fìsica d'Altes Energies. Unpublished, (1993).

[9] ALEPH Collab. D.Camp *et al.*, Phys.Lett. **B346** (1995) 379.

[10] Y.S.Tsai, Phys. Rev. **D4** (1971) 2821.

[11] S.Jadach , J.H.Kuhn and Z.Wąs, Comp.Phys.Commun. **64** (1991) 275.

[12] S. Jadach and Z. Wąs, Acta Phys. Polon. **B15** (1984) 1151.

[13] W.Fetscher, Phys. Rev. **D42** (1990) 1544.

[14] S.Goozovat and C.A.Nelson, Phys. Review **D44** (1991) 2818.

[15] R.Alemany, N.Rius, J.Bernabeu,J.J. Gómez-Cadenas, A.Pich: Nucl.Phys. **B379**, (1992) 3.

[16] Particle Data Group, R.M.Barnett et al., Review of Particle Properties, Phys. Rev. **D54** (1996).

[17] F.Sánchez, Phys.Lett. **B384** (1996) 277.

[18] Chris Bowdery, " ALEPH Handbook Vol.1", ISBN 92-9083-072-7.
ALEPH Collab., Buskulic et al.,"Performance of the ALEPH detector at LEP", Nucl. Inst. and Meth. **A360** (1995) 481.
ALEPH Collab., D.Decamps et al., Nucl. Inst. and Meth. **A294** (1990) 121.

[19] G. Batignani et al., 1991 IEEE Nuclear Science Symposium, Santa Fe, IEEE Trans. Nucl. Sci. NS-39(4/5) (1992) Vol.1 p. 438.

[20] G.J.Barber et al., Nucl. Inst. and Meth. **A279** (1989) 212.

[21] W.B.Atwood et al., Nucl. Inst. and Meth. **A306** (1991) 446.

[22] D.Bederede et al., Nucl. Inst. and Meth. **A365** (1995) 117.

[23] E.Fernández et al., Nucl. Inst. and Meth. **A297** (1990) 153.

[24] M.Delfino et al., Comp. Phys. Comm. **57** (1989) 401.

[25] ALEPH Collab. D.Buskulic *et al.*, Z.Phys. **C70** (1996) 561.

[26] ALEPH Collab. D.Buskulic *et al.*, Z.Phys. **C70** (1996) 579.

[27] W.Hollik, "Predictions for e^+e^- Processes", MPI-Ph/93-22, BI-TP 93/33
R.Miquel, "Radiative Corrections to the Process $e^+e^- \to \nu\nu\gamma$", Ph.D. thesis, Universitat Autónoma de Barcelona, unpublished, (1989).

[28] S.Jadach, B.F.L. Ward and Z.Wąs, Comp.Phys.Commum. **79** (1994) 503.

[29] The LEP Collaborations ALEPH, DELPHI, L3, OPAL and the LEP Electroweak Working Group, "A combination of Preliminary LEP Electroweak Measurements and Constrain of the Standard Model", CERN-PPE/95-172.

[30] ALEPH Collaboration, D.Buskulic et al., Phys. Lett. **B297**, 459 (1992),
ALEPH Collaboration, D.Buskulic et al., Phys. Lett. **B346**, 371 (1995),
ALEPH Collaboration, D.Buskulic et al., Paper contribution to Warsaw conference, **PA08-030** (1996)
OPAL Collaboration, P.D.Acton et al., Phys.Lett. **B281**,(1992) 405
OPAL Collaboration, P.D.Acton et al., Z.Phys. **C66**, 405(1995) 31

[31] U.Stiegler, Z. Phys. **C58**, (1993) 601.

[32] U.Stiegler, Z. Phys. **C57**, (1993) 511.